Remote Sensing of Environment 302 (2024) 113970

Contents lists available at ScienceDirect

Remote Sensing of Environment

journal homepage: www.elsevier.com/locate/rse

First mapping of polarization-dependent vegetation optical depth and soil moisture from SMAP L-band radiometry

Zhiqing Peng [a,b], Tianjie Zhao [a,*], Jiancheng Shi [c], Lu Hu [d], Nemesio J. Rodríguez-Fernández [e], Jean-Pierre Wigneron [f], Thomas J. Jackson [g], Jeffrey P. Walker [h], Michael H. Cosh [i], Kun Yang [j], Hui Lu [j], Yu Bai [a,b], Panpan Yao [a], Jingyao Zheng [k], Zushuai Wei [l]

[a] State Key Laboratory of Remote Sensing Science, Aerospace Information Research Institute, Chinese Academy of Sciences, Beijing 100101, China
[b] University of Chinese Academy of Sciences, Beijing 100049, China
[c] National Space Science Center, Chinese Academy of Sciences, Beijing 100190, China
[d] International Institute for Earth System Science, Nanjing University, Nanjing 210023, China
[e] Centre d'Etudes Spatiales de la Biosphère (CESBIO), Université de Toulouse, Centre National d'Etudes Spatiales (CNES), Centre National de la Recherche Scientifique (CNRS), Institut de Recherche pour le Dévelopement (IRD), Université Paul Sabatier, Institut National de Recherche pour l'Agriculture, l'Alimentation et l'Environnement (INRAE), 18 av. Edouard Belin, bpi 2801, 31401 Toulouse, France
[f] INRAE, UMR 1391 ISPA, Universit'e de Bordeaux, F-33140 Villenave d'Ornon, France
[g] United States Department of Agriculture, Agricultural Research Service, Hydrology and Remote Sensing Laboratory (Retired), MD 20705-2350, United States
[h] Department of Civil Engineering, Monash University, Clayton 3800, Australia
[i] United States Department of Agriculture, Agricultural Research Service, Hydrology and Remote Sensing Laboratory, Beltsville, MD 20705-2350, USA
[j] Department of Earth System Science, Tsinghua University, Beijing 100084, China
[k] State Key Laboratory of Hydrology-Water Resources and Hydraulic Engineering, National Cooperative Innovation Center for Water Safety and Hydro-science, College of Hydrology and Water Resources, Hohai University, Nanjing 210024, China
[l] School of Artificial Intelligence, Jianghan University, Wuhan 430056, China

ARTICLE INFO

Edited by Jing M. Chen

Keywords:
Soil moisture
Vegetation optical depth
MCCA
Polarization dependence
SMAP

ABSTRACT

Soil moisture (SM) and vegetation optical depth (VOD) estimates using passive microwave remote sensing at L-band (1.4 GHz) are essential for attaining a better understanding of water exchanges at the land-atmosphere interface. However, current retrieval algorithms often ignore the polarization dependence of vegetation effects. This study proposed a parameter self-calibrating framework for the multi-channel collaborative algorithm (MCCA) and presented a new SM and the first polarization-dependent VOD product based on the dual-polarized L-band observations at a fixed angle (40°) from the NASA Soil Moisture Active Passive (SMAP) mission. The parameter self-calibrating framework utilizes an information theory-based approach to obtain surface roughness and effective scattering albedo globally. Furthermore, the MCCA does not require auxiliary data for vegetation or soil moisture to constrain the retrieval process. Comparison with other SM and VOD products, such as MT-DCA version 5, DCA, SCA-H, SCA-V from SMAP Level-3 products version 8, and SMAP-IB, demonstrate analogous spatial patterns. The MCCA-derived SM exhibits the lowest unbiased root mean square deviation (ubRMSD, about 0.055 m^3/m^3), followed by SMAP-IB and DCA (0.061 m^3/m^3), with an overall Pearson's correlation coefficient of 0.744 (SMAP-IB performed best with $R = 0.764$) when evaluated against *in-situ* observations from 18 dense soil moisture networks. The MCCA generates VOD values for both vertical and horizontal polarization, demonstrating a slight polarization difference of vegetation effect at the satellite scale. Both VODs exhibit a strong linear relationship with above-ground biomass and canopy height. The polarization difference of VODs is primarily observed in densely vegetated and arid areas.

1. Introduction

Soil moisture (SM) is an important boundary condition of land-atmosphere feedbacks (Green et al., 2019), and is identified as an essential climate variable by the Global Climate Observing System (GCOS-138, 2010). Vegetation optical depth (VOD, τ) is a physical

* Corresponding author.
E-mail address: zhaotj@aircas.ac.cn (T. Zhao).

https://doi.org/10.1016/j.rse.2023.113970
Received 12 September 2023; Received in revised form 17 November 2023; Accepted 18 December 2023
Available online 26 December 2023

variable that describes the microwave extinction effects caused by vegetation in the microwave radiative transfer models (RTM) (Mo et al., 1982; Ulaby and Wilson, 1985) and it provides information on both plant water status (Konings et al., 2021) and biomass (Fan et al., 2019; Liu et al., 2015). Microwave remote sensing has good capability to retrieve SM and VOD (Karthikeyan et al., 2017; Wigneron et al., 2017), especially passive microwave L-band (1–2 GHz) because at these wavelengths the vegetation is semi-transparent, and the observed brightness temperature (Tb) is sensitive to the water content of the first few centimeters of the soil surface, and absorption and scattering have lower impacts, compared to shorter wavelengths (Hornbuckle et al., 2016).

Current L-band passive microwave sensors on Earth-orbiting satellites include the European Space Agency's (ESA) Soil Moisture and Ocean Salinity (SMOS) mission, launched in November 2009 with multi-angular and full-polarized observations (Kerr et al., 2010) and the National Aeronautics and Space Administration's (NASA) Soil Moisture Active Passive (SMAP) mission, launched in January 2015 with full-polarized observations at an incidence angle of 40° (Entekhabi et al., 2010a). This study focuses on the retrieval of SM and VOD using SMAP observations.

Most SM and VOD retrieval algorithms for SMAP are based on the zero-order solution of RTM, also known as the τ-ω model. They can be categorized into three types (Zhao et al., 2021):

(1) Algorithms based on the reverse-order RTM: SM is directly derived from the surface soil roughness and dielectric model, with VOD estimated by introducing auxiliary data from optical vegetation indices (Jackson, 1993). For example, the single channel algorithm (SCA), either at horizontal (SCA-H) or vertical (SCA-V) polarization, uses the normalized difference vegetation index (NDVI) as a proxy of vegetation water content (VWC) in the SMAP SM products (O'Neill et al., 2021a). The retrieval performance is dependent on the uncertainties introduced by the auxiliary data (Zhao et al., 2014).

(2) Iterative algorithms based on forward simulations of RTM: One such algorithm is the dual-channel algorithm (DCA) (Chan et al., 2018; Chaubell et al., 2020; O'Neill et al., 2021a), which iteratively minimizes a cost function using nonlinear least-squares to retrieve SM and VOD. Since SMAP provides only two observations during an overpass, the degree of information (DoI) of Tbs can be lower than the number of unknowns (surface parameters, SM, and VOD) (Konings et al., 2015). These algorithms may incorporate prior spatial or temporal information or apply regularization techniques to enhance the robustness of the retrievals (Gao et al., 2021). For example, Konings et al., (2016, 2017) proposed a multi-temporal dual-channel algorithm (MT-DCA) to retrieve SM, VOD, and effective single scattering albedo (ω, omega) by assuming that VOD is constant in the multi-temporal overpass during the retrieval process. SMAP-INRAE-BORDEAUX (SMAP-IB) uses multi-temporal averages of SM and VOD in the cost function to constrain the retrieval (Li et al., 2022). Another algorithm uses the two-stream model and spatial information to assume VOD as constant over a limited area for retrieving SM, VOD, and ω, simultaneously (Gao et al., 2020b). Additional constraint methods add a regularization term in the cost function (Zwieback et al., 2019), which could smooth short-term variability and reduce retrieval uncertainty (Feldman et al., 2021b). This kind of variant algorithm of DCA is applied to SMAP including the constrained multi-channel algorithm (CMCA) (Ebtehaj and Bras, 2019), and the combined CMCA (C-CMCA) (Gao et al., 2020a).

(3) Algorithms based on microwave indices: These algorithms establish analytical relationships between microwave observations and geophysical variables for retrieval purposes (Lu et al., 2009; Njoku and Chan, 2006). For example, the land parameter retrieval model (LPRM) expresses the microwave polarization difference index (MPDI) analytically as a function of SM and VOD (Meesters et al., 2005; Owe et al., 2001). LPRM has also been employed in SMAP (O'Neill et al., 2021a).

Most of these algorithms ignore the discrepancy of vegetation characteristics between polarizations (the SMAP SCA recognizes this by using different parameter sets for H- and V-polarization). The τ-ω model is the zero-order approximation of the RTM. The vegetation-related parameters ω and VOD are effective (equivalent) values (Kurum, 2013), which are theoretically affected by incidence angle, polarization, frequency, and ground reflectivity. The polarization and incidence angle dependence of VOD depends on the structure of the vegetation and the distribution of liquid water within those structures, and it is not necessarily the same for different types of vegetation or even for different phenological stages of a given type of vegetation. For the satellite footprint scale, researchers hypothesize that the polarization dependence of VOD is weak because a variety of vegetation and soil types is included in a satellite footprint of tens of kilometers (Njoku and Li, 1999; Owe et al., 2001; Wigneron et al., 2017). Operational algorithms neglect the VWC distribution variations with vegetation (Konings et al., 2021; Xu et al., 2021). Moreover, the difference between VOD at H- and V-polarization is ignored (Baur et al., 2019; Kerr et al., 2012; Wigneron et al., 2017). These simplifications might induce uncertainties in the retrieval of VOD, affect the subsequent analysis, and result in a missed opportunity for a better understanding of VOD (Konings et al., 2021). It is worth noting that VOD dependence on polarization has been commonly found and investigated in previous ground-based experiments for several vegetation types (Brunfeldt and Ulaby, 1984; Wigneron et al., 1995; Wigneron et al., 2004). For L- and C-band, Van de Griend et al. (1996) found that H-polarized VOD is generally smaller than V-polarized VOD at different incidence angles in wheat crop fields. Wigneron et al. (2004) found a large VOD polarization discrepancy based on several experimental datasets collected at the L-band, particularly for crops with vertical structures (wheat, corn). Schwank et al. (2005) demonstrated and simulated polarization-dependent VOD for fast-changing vegetation structure due to a hail event. Ground-based radiometer measurements in the Soil Moisture Experiment in the Luan River (SMLER) showed that the L-band vegetation attenuation coefficient b (VOD = b•VWC) of H- and V-polarization changes alternately with the incidence angles (b of H-polarization is not always smaller than b of V-polarization) in a crop field (Zhao et al., 2020). Currently, few published results explore the polarization difference of satellite VOD for SMAP. Hence, there is a need to further investigate the SMAP VOD dependence on polarizations for a better understanding of the associated vegetation properties.

More recently, a new algorithm named the multi-channel collaborative algorithm (MCCA) was developed to retrieve SM and microwave-channel-dependent VOD (Zhao et al., 2021), where the multiple channels refer to different frequencies, polarizations, and incidence angles. In the case of SMAP, which operates at L-band only, it has two channels: H- and V-polarized Tbs at 40°. To implement the MCCA, one channel (H-/V-polarization) is selected as the core channel, and the other (V-/H-polarization) as the collaborative channel, H-polarization was selected as the core channel in this study. The main idea of the MCCA is to apply the relationship between soil and vegetation properties of the core channel to the collaborative channel using three features: (1) unlike other algorithms using proxy or iterative procedure to retrieve VOD, an analytical solution was proposed to derive the vegetation transmissivity followed by VOD; (2) a general function was proposed to describe the relationships of VODs between microwave-channels; and (3) The relationship between the Tbs of the core and the collaborative channel was derived from the two-component version of the τ-ω model and used to estimate the Tb of the collaborative channel. Given that SMAP has only two channels, it is challenging to enhance the capability of retrieving polarization-dependent VOD from SMAP data without ancillary data.

In this study, a parameter self-calibrating framework is proposed for retrieving both SM and VOD using the MCCA algorithm with SMAP data. The main objectives of this research were as follows: (1) to assess the feasibility of the MCCA algorithm for retrieving SM and VOD with only two observations at the satellite scale; (2) to minimize the reliance on ancillary data associated with SMAP in the retrieval of SM and VOD in SMAP official algorithms; and (3) to estimate polarization-dependent

VOD at L-band using SMAP data. The primary focus of this paper is to present the further development of the MCCA algorithm for retrieving SM and VOD using SMAP data and to conduct an inter-comparison of the global SM and VOD products from SMAP-IB (Li et al., 2022), MT-DCA (Feldman et al., 2021a), and the three released official SMAP radiometer products (DCA, SCA-H, and SCA-V) (O'Neill et al., 2021a; O'Neill et al., 2021b).

2. Dataset

2.1. SMAP Level-3 brightness temperature product

The SMAP satellite is in a sun-synchronous orbit, with ascent and descent over the equator at 6:00 PM and 6:00 AM local solar time, respectively. SMAP has a swath width of about 1000 km, and its average coverage period is 1–3 days. It scans the Earth with an incidence angle of 40°. In this study, H- and V-polarized Tb, and the surface temperature included in the SMAP Level-3 Radiometer Global Daily 36 km EASE-Grid Soil Moisture (SPL3SMP) version 8 were used to retrieve SM and VOD. The SPL3SMP is distributed by the National Snow and Ice Data Center (NDISC) and projected to the global Equal-Area Scalable Earth-2 (EASE2) grid with a spatial sampling of 36-km (O'Neill et al., 2021b). ω and the surface roughness parameter in SPL3SMP were not used. The SMAP SM and VOD products based on the DCA, SCA-H, and SCA-V in SPL3SMP were also used to inter-compare with the MCCA retrieved SM and VOD.

2.2. Soil moisture networks

Due to the heterogeneity of satellite footprints, 19 dense networks and 1 sparse network (the soil climate analysis network, SCAN) (Schaefer et al., 2007) were involved to evaluate MCCA and the other five remotely sensed SM estimates, including (a) eight networks (SCAN, HOBE, MySMNet, REMEDHUS, Yanco, Kyeamba, TERENO, and SMN-SDR) sourced from the International Soil Moisture Network (ISMN) database (Dorigo et al., 2011); (b) data for seven networks (South Fork, Walnut Gulch, St. Joseph's, Reynolds Creek, Fort Cobb, Little Washita, and Little River) was obtained from the United States Department of Agriculture (USDA) (Jackson et al., 2012), (c) four additional networks (Shiquanhe, Maqu, Naqu, and Pali) were accessed from the National Tibetan Plateau Data Center, and (d) the SMN-WDL network built in the Tibet Plateau, focuses on observing soil moisture, soil temperature, and freeze/thaw state (Zheng et al., 2024). Basic information about these networks can be found in Table 1, with additional details available in Table S1 in the supplementary material.

2.3. Other datasets

Sand and clay fractions were obtained from the global soil texture database (SoilGrids250m) for use in the dielectric model (Hengl et al., 2017). VWC has a significant impact on VOD and is closely related to biomass and canopy height. For comparative analysis, retrieved VOD from MCCA and other algorithms, was assessed against global ecosystem dynamics indicators. Canopy height data were collected from the global ecosystem dynamics investigation (GEDI) Level 3 gridded mean canopy height (version 2) (Dubayah et al., 2021), while above-ground biomass (version 4) was sourced from the ESA Climate Change Initiative (CCI) Programme (Santoro and Cartus, 2023) were utilized. Total precipitation data from the ERA5-Land hourly data (Muñoz Sabater, 2019), converted from hourly to a daily sum, were also used in the analysis. Frozen precipitation was also considered as it contributes to SM. All datasets were aggregated to align with the SMAP pixel grid size. Additionally, a tree cover map derived from 3-m spatial resolution Planetscope images in Africa was used to analyze the VODs in the Sahara deserts (Reiner et al., 2023a). This tree cover map provided detailed information on tree distribution and density at a spatial resolution of

Table 1
The dense soil moisture networks information.

Network name	Country	Climate regime	Depth (cm)	Sensor numbers	Data period used	Network name	Country	Climate regime	Depth (cm)	Sensor numbers	Data period used
HOBE	Denmark	Temperate	0–5	27	2015/03/31–2019/03/13	Fort Cobb	USA	Temperate	5	14	2015/03/31–2019/03/04
MySMNet	Malaysia	Tropical	0–5	7	2015/03/31–2015/12/31	Little Washita	USA	Temperate	5	19	2015/03/31–2019/03/25
REMEDHUS	Spain	Temperate	0–5	20	2015/03/31–2019/01/01	Little River	USA	Temperate	5	29	2015/03/31–2018/07/19
Yanco	Australia	Semi-Arid	0–5	12	2015/03/31–2018/08/27	Shiquanhe	China	Cold	5	12	2015/03/31–2019/08/31
Kyeamba	Australia	Temperate	0–5	7	2015/03/31–2018/08/27	Maqu	China	Cold	5	16	2015/03/31–2019/05/31
TERENO	Germany	Temperate	5	4	2015/03/31–2019/04/03	Naqu	China	Polar	0–5	44	2015/03/31–2018/10/15
Walnut Gulch	USA	Arid	5	29	2015/03/31–2019/12/31	Pali	China	Tundra	0–5	17	2015/06/20–2018/10/10
St. Joseph's	USA	Cold	5	10	2015/03/31–2019/02/27	SMN-SDR	China	Continental	3	34	2018/09/11–2021/05/07
South Fork	USA	Cold	5	20	2015/03/31–2018/12/31	SMN-WDL	China	Polar	5	10	2019/09/19–2021/11/17
Reynolds Creek	USA	Arid	5	18	2015/03/31–2018/02/20	SCAN	USA	–	5	134	2015/04/02–2021/03/30

Sensor numbers refer to the maximum station of a network in the validation period, if two sensors are installed at the same location (same longitude and latitude, but different sensors), it is treated as one.

100 m.

To compare the results of MCCA, SMAP SM and VOD products from MT-DCA (Konings et al., 2017) version 5 (Feldman et al., 2021a), and SMAP-IB (Li et al., 2022) were utilized.

3. Methodology

3.1. Multi-channel collaborative algorithm

MCCA is based on the two-component version of the τ-ω model proposed by Shi et al. (2008), which for SMAP is written as:

$$Tb_P = V_P^e + V_P^t \bullet e_P^s, \tag{1}$$

where subscript P stands for polarization (H- or V-), superscript s stands for soil surface, e_P^s is emissivity of rough soil surface, V_P^e is the vegetation emission term, and $V_P^t$is the vegetation transmission term. The variables V_P^e and V_P^t can be calculated as:

$$V_P^e = e_P^v \bullet (1 + \Gamma_P) \bullet T^v, \tag{2}$$

$$V_P^t = \Gamma_P \bullet T^s - e_P^v \bullet \Gamma_P \bullet T^v, \tag{3}$$

where superscript v stands for vegetation, T^s and T^v are physical temperatures of the vegetation and soil, respectively, Γ_P is vegetation transmissivity, e_P^v is the vegetation emissivity that can be expressed as $(1-\omega_P) \bullet (1-\Gamma_P)$, and ω_P is the single scattering albedo. MCCA needs at least two channels in the retrieval procedure. Among them, one channel is set as the core channel, and the others are set as collaborative channels. H-polarization was set as the core channel in this study. The Tb at V-polarization can therefore be written as an equation of Tb at H-polarization without any assumptions such that:

$$Tb_V = V_V^e - S_r V_r \bullet V_H^e + S_r V_r \bullet Tb_H, \tag{4}$$

where $S_r = \frac{e_V^s}{e_H^s}$ is the ratio of soil emissivity as a function of SM and surface roughness (*Rou*); and $V_r = \frac{V_V^t}{V_H^t}$ is the ratio of the vegetation transmission term, more details can be found from the supplementary material in Zhao et al. (2021).

Given Tb for a specific channel (H or V) and rearranging eqs. (1)–(3), the τ-ω model can be written as:

$$a' \bullet \Gamma_P^2 + b' \bullet \Gamma_P + c' = 0, \tag{5}$$

with parameters a', b', c' defined as:

$$a' = -\left(1 - e_P^s\right) \bullet (1 - \omega_P) \bullet T^v, \tag{6}$$

$$b' = e_P^s \bullet [T^s - (1 - \omega_P) \bullet T^v], \tag{7}$$

$$c' = (1 - \omega_P) \bullet T^v - Tb_P^v, \tag{8}$$

where Tb_P^v is the Tb emitted from vegetated areas. Importantly, $a' + c' < 0$ indicates a vegetated area, and $a' + c' = 0$ indicates a bare soil. Moreover, the analytical solution of the general quadratic eq. (5) can be used to derive Γ_P as:

$$\Gamma_P = \frac{-b' \pm \sqrt{b'^2 - 4 \bullet a' \bullet c'}}{2 \bullet a'}, \tag{9}$$

and VOD can be calculated according to Beer's law:

$$VOD_P = -ln(\Gamma_P) \bullet cos\theta, \tag{10}$$

where θ is the incidence angle (observation angle relative to nadir at ground) of SMAP.

For certain vegetation properties, the electromagnetic radiation at different channels will interact with different parts of the vegetation (water content), thus leading to different VODs, which can be described using the general function F_{asm} proposed by Zhao et al. (2021) based on previous studies (Jackson and Schmugge, 1991; Wigneron et al., 1995), given as:

$$F_{asm}: \frac{VOD_H}{VOD_V} = \left(\frac{f_H}{f_V}\right)^{C_f} \bullet \frac{sin^2\theta \bullet C_H + cos^2\theta}{sin^2\theta \bullet C_V + cos^2\theta}, \tag{11}$$

Because SMAP has only L-band observations at 40°, the frequency and incidence angle dependent component are ignored, and F_{asm} can be simplified as:

$$F_{asm}: \frac{VOD_H}{VOD_V} = \frac{sin^2 40 \bullet C_H + cos^2 40}{sin^2 40 \bullet C_V + cos^2 40}, \tag{12}$$

where C_H and C_V are parameters characterizing the dependence of VOD on polarizations, respectively. They were set as 1 in the current MCCA SMAP SM retrieval procedure.

Because SMAP only has two channels, it is challenging to incorporate the polarization dependence of every related parameter without the use of ancillary data. Therefore, the polarization dependence of ω is not considered in this study. When given ω, roughness parameter, and SM values, the corresponding VOD can be calculated from the Tb at H-polarization (core channel) by eqs. (9) and (10), and the Tb at V-polarization (collaborative channel) can be estimated by eq. (4), with VOD at V-polarization calculated by eq. (12). The estimated Tb at V-polarization is then utilized to choose the best SM value by minimizing the cost function Φ such that:

$$min\Phi = \frac{\left(Tb_V^{estimated} - Tb_V^{observed}\right)^2}{Tb_V^{observed}}, \tag{13}$$

where $Tb_V^{estimated}$ is the Tb estimated by eq. (4), and $Tb_V^{observed}$ is the observed Tb at V-polarization. Finally, once the SM is retrieved, VODs at H- and V-polarizations can be calculated by eqs. (9) and (10). The flowchart of MCCA is shown in Fig. 1, which can be implemented in both ergodic form and iterative form (Zhao et al., 2021). To reduce the usage of auxiliary data, the ergodic form of MCCA was implemented in this study, in which a series of SM values from 0.001 (unit: m^3/m^3) to porosity (the fraction of void space in the soil, unit: m^3/m^3) were set as input.

3.2. Advancement of the algorithm for parameter self-calibrating

The successful implementation of MCCA with SMAP data hinges on the calibration of ω and *Rou* at L-band, based on only two SMAP Tb observations and the fact that using the τ-ω model it is difficult to disentangle the scattering albedo from the soil roughness effect (Wigneron et al., 2017). To address this challenge, a self-calibrating framework was proposed that fine-tunes algorithm parameters through the utilization of time-series Tb observations while leveraging an information theory-based strategy.

Information theory has played a significant role in the field of remote sensing, offering valuable insights and techniques. For example, Wang and Bras (2011) proposed a model for estimating evapotranspiration based on the theory of maximum entropy production. Similarly, entropy has been employed in the design of soil moisture monitoring networks, such as the SMOS L3 SM study conducted by Kornelsen and Coulibaly (2015), as well as the development of an improved AGB model as demonstrated by Adnan et al. (2021). In this study, two information theory metrics are employed, namely the degree of information (*DoI*) and the Wasserstein distance, to determine the appropriate values for ω and *Rou*, respectively. The minimal *DoI* can give a relatively high coefficient of correlation value with relatively reasonable ω, and the minimal Wasserstein distance tends to find SM with low values of ubRMSD based on the test on the *in-situ* observations, more details can be found in Fig. S1 in the supplement. Accordingly, the usage of these

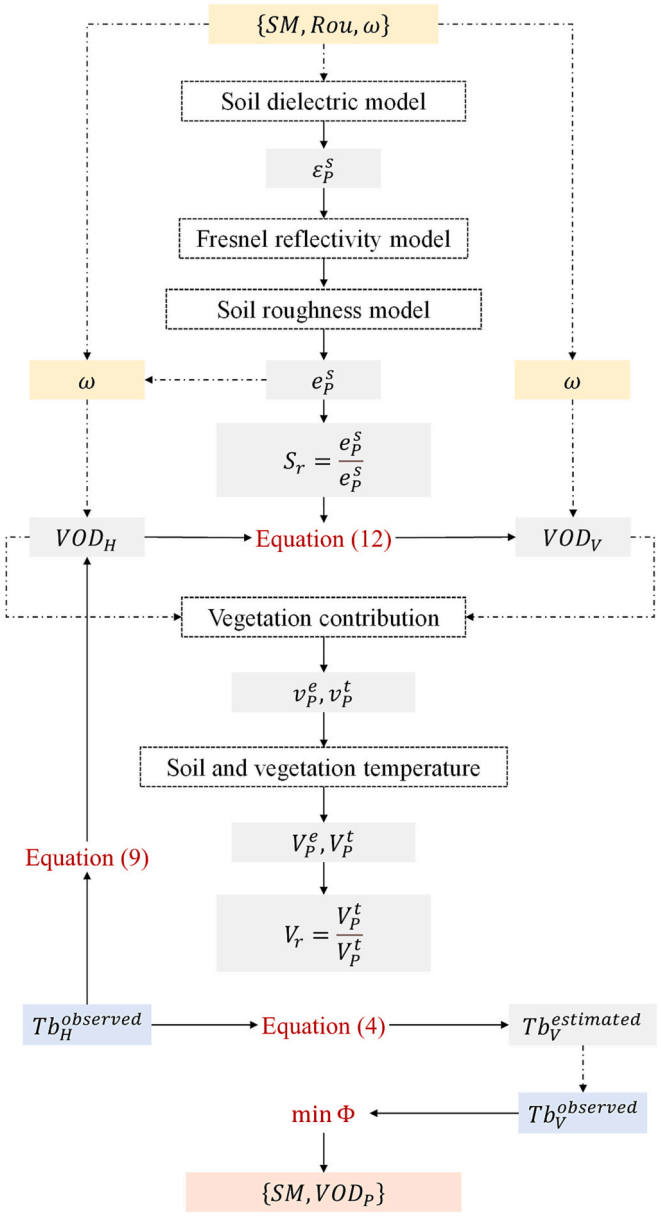

Fig. 1. Flowchart of the MCCA, adapted from the flowchart in Zhao et al. (2021).

two metrics is first introduced, with data from 2016 to 2018 used as an example to demonstrate the parameter self-calibrating framework.

The *DoI* has been proposed by Konings et al. (2015) for quantifying the number of parameters that can be robustly retrieved from a given dataset. Accordingly, this study has utilized the *DoI* to assess the independent information between SM and VOD. To optimize the value of ω within the range of 0 to 0.2, with a step of 0.001, a minimum *DoI* approach at each given *Rou* was employed according to:

$$DoI = N - \frac{T(SM, VOD)}{H(SM, VOD)}, \tag{14}$$

where N is 2 (because SM and VOD are two independent variables); $T(SM, VOD)$ is the total correlation quantifying the amount of dependence among SM and VOD, and $H(SM, VOD)$ is the joint entropy, expressed as:

$$H(SM, VOD) = -\sum_{SM}\sum_{VOD} p(SM, VOD) \bullet log_2 p(SM, VOD), \tag{15}$$

$$T(SM, VOD) = H(SM) + H(VOD) - H(SM, VOD), \tag{16}$$

where $p(SM, VOD)$ is the joint probability mass function (pmf) of SM and VOD, $H(SM)$ and $H(VOD)$ are the Shannon entropy of SM and VOD, respectively (Cover and Thomas, 2005), and $H(SM)$ is described as:

$$H(SM) = -\sum p(SM) log_2 p(SM), \tag{17}$$

where $p(SM)$ is the pmf of SM. The equation of $H(VOD)$ is not listed above because its form is the same as $H(SM)$. The calculation of entropy is affected by the choice of bin size, so Scott's rule (Scott, 1979) was employed to determine the bin size, as suggested by Konings et al. (2015). However, it is important to note that Scott's rule is influenced by the standard deviation and size of the data. To ensure the stability of *DoI* values, it is preferable to utilize a larger dataset, *DoIs* at different ω for a given *Rou* shared the same bin size calculated from the whole set. Furthermore, employing the same bin size configuration allowed for the comparability of *DoIs* at the same level. It is important to clarify that SM and VOD are two distinct quantities with no inherent dependence. Although VOD is related to SM through the total Tb of a vegetated surface, as calculated using eqs. (1) and (4), the calibration of ω based on minimum *DoI* does not imply an interdependence between SM and VOD.

The parametric surface roughness model proposed by Zhao et al. (2015) was used to characterize the impact of surface roughness with the specification of an exponentially correlated surface. This model proposed a parameter *Rou* based on geometric roughness variables ($Rou = \frac{s^2}{l}$, root mean square height s and correlation length l, in centimeters) to represent surface roughness and was separately parameterized for H- and V-polarizations. For a given ω, the minimum Wasserstein distance (*WD*) between SM and VOD was used to determine *Rou* according to Ramdas et al. (2017):

$$WD(p, q) = \inf_{\gamma \in \prod(p,q)} \int_{\mathbb{R}\times\mathbb{R}} |SM - VOD| d\gamma(SM, VOD), \tag{18}$$

where $\prod(p, q)$ represents the set of all couplings of p and q, a coupling γ is a joint probability measure on $\mathbb{R} \times \mathbb{R}$ whose marginals are p, q on SM and VOD, respectively. The Wasserstein distance is a distance function defined between probability distributions on a given metric space and has been widely used as a loss function in deep learning like generative adversarial networks (Arjovsky et al., 2017; Gulrajani et al., 2017). To determine the optimal *Rou*, a range of [0, 4.5] with a step of 0.01 was considered for a given ω, and the minimum Wasserstein distance was utilized as a criterion for selection.

SMAP Tbs from the period of 2016 to 2018 were utilized in this study to calibrate *Rou* and ω on a global scale. The parameter self-calibrating framework was performed for each pixel, following the flowchart presented in Fig. 2.

The self-calibrating of *Rou* was carried out under two extreme conditions. For the first condition, which was assumed a smooth surface, the following procedure was followed:

(1) *Rou* was initially set to 0 globally. Using the MCCA algorithm, 201 pairs of SM and VOD at H and V polarizations were retrieved fora range of ω from 0 to 0.2 with a step of 0.001. The bin size for *DoI* calculation was determined using all the 201 pairs of time series SM and H-polarized VOD. The ω value corresponding to the minimum *DoI* was selected as the result.

(2) With the ω value obtained from step (1), 451 pairs of time series SM and VOD were retrieved using MCCA for *Rou* values ranging from 0 to 4.5 with a step of 0.01. The first initial *Rou* (Rou_{init1}) was optimized by minimizing the *WDs* calculated by SM and VOD at H-polarization.

For the second condition, which assumed no vegetation scattering, the second initial *Rou* (Rou_{init2}) was optimized using the same procedure as step (2) in the first condition, but with ω fixed at 0.

Extreme value-based parameter estimation is frequently utilized in remote sensing-based algorithms. Two well-known examples of such

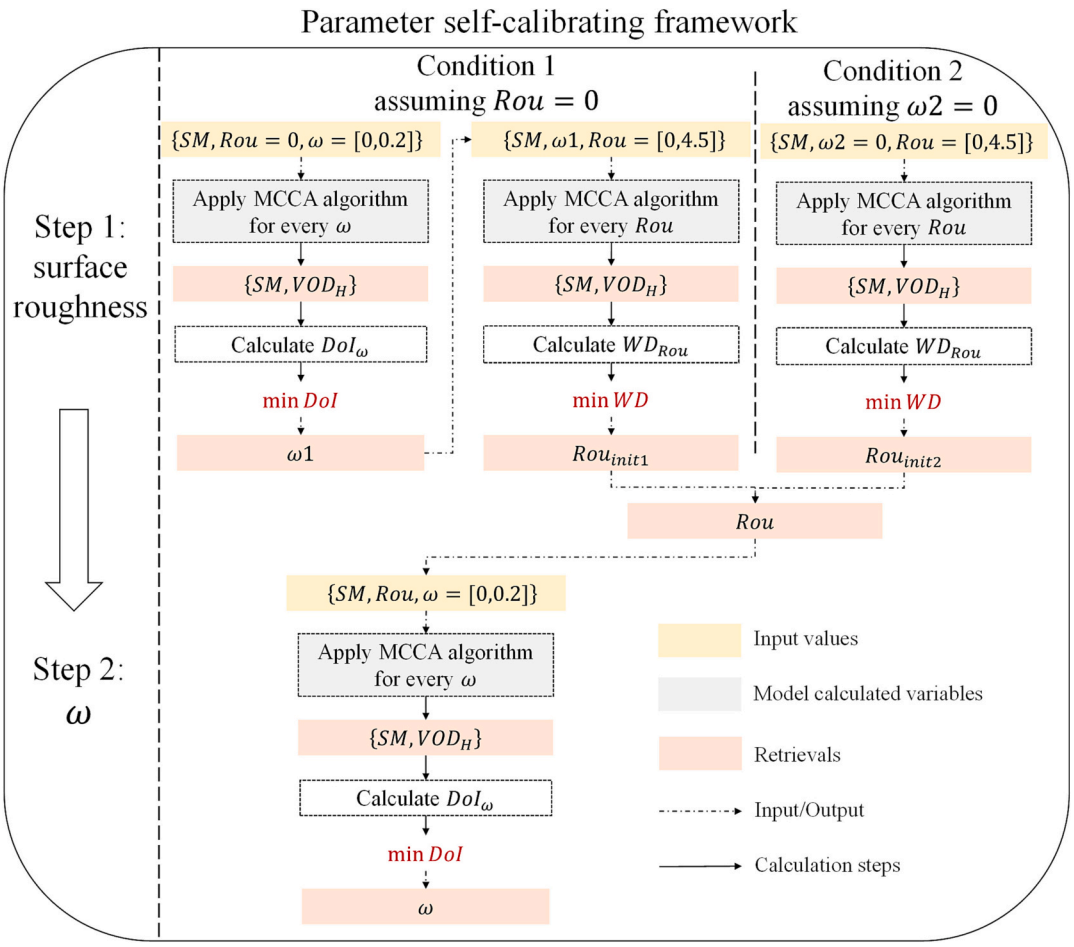

Fig. 2. Flowchart of procedure for self-calibration of *Rou* and ω.

algorithms are the surface energy balance system (Su, 2002) and the surface energy balance algorithm for land (Bastiaanssen et al., 1998). The final *Rou* value used in the retrieval process was calculated as the simple arithmetic average of the two initial *Rou* values at extreme conditions, according to:

$$Rou = (Rou_{init1} + Rou_{init2})/2, \quad (19)$$

The spatial distribution and boxplot of *Rou* are shown in Fig. 3. To a certain extent, the retrieved *Rou* shows topographical features from mountainous areas like the Himalayan Mountains in Asia and the Tibesti Mountain in the Sahara Desert. The spatial pattern of *Rou* is analogous to that of the roughness parameter in the SMAP DCA algorithm (Chaubell et al., 2020) and the global roughness map estimated from the SMOS data in 2011, as reported in Parrens et al. (2016), and roughness obtained from the Advanced Microwave Scanning Radiometer for Earth Observing System (AMSR-E) (Karthikeyan et al., 2019). However, surface roughness is not only due to topography but also due to other kinds of small-scale heterogeneities in ground permittivity (Schwank et al., 2010). Large *Rou* values are observed in dense vegetation regions, such as tropical forests (*e.g.*, Amazon in Brazil, Congo Basins, and South-East Asia) and boreal forests at high latitudes. The high *Rou* values in dense vegetation regions may be attributed to the presence of ground litter lying at the bottom of the canopy, which affects microwave emission but is not accounted for in the RTM of this study. It is consistent with previous literature that found high roughness effects in forested areas (Grant et al., 2008; Grant et al., 2007; Parrens et al., 2016).

The final ω was calibrated by repeating step (1) of calibrating *Rou*, but with the constant *Rou* value replaced by the final *Rou* value. Fig. 4(a) displays the global map of ω, having a similar spatial pattern to the averaged time series of ω retrieved in Baur et al. (2021) and the ω map obtained by MT-DCA in Konings et al. (2017). Fig. 4(b) shows that forests tend to have higher ω values compared to other classifications. This is because scattering increases in larger and more complex canopies (Baur et al., 2021). Only 6% of the pixels attained $\omega > 0.15$. These pixels were mostly in water bodies (45.8%), and so could be filtered based on the water fraction. Additionally, 13% of the pixels with high ω values were associated with grasslands, primarily located in the far northern regions of Canada and the Tundra, where significant water bodies are present, which aligns with the result from MT-DCA in Konings et al. (2017).

3.3. Evaluation methods

The comparison of MCCA retrieved SM and VOD with five other products was conducted during the same period, specifically at the overpass of local 6:00 AM because MT-DCA and SMAP-IB only provide descending data. This comparison was conducted globally, encompassing both SM and VOD data over three consecutive years from 2016 to 2018. The following steps were taken in the process: (a) removal of outliers falling outside the range of Q1–1.5•IQR and Q3 + 1.5•IQR, where Q1 and Q3 are the first and third quantiles, and IQR is the interquantile range (Q3-Q1); (b) exclusion of pixels with <30 data samples; and (c) elimination of other products when "Scene Flags" > 1 and "Soil_Moisture_StdError" > 0.05 in SMAP-IB during the validation of SM at networks, following the SMAP-IB product recommendations. Additionally, "Optical_Thickness_Nad" >0.05 in SMAP-IB was also used to exclude VOD data when comparing the global pattern of these six products.

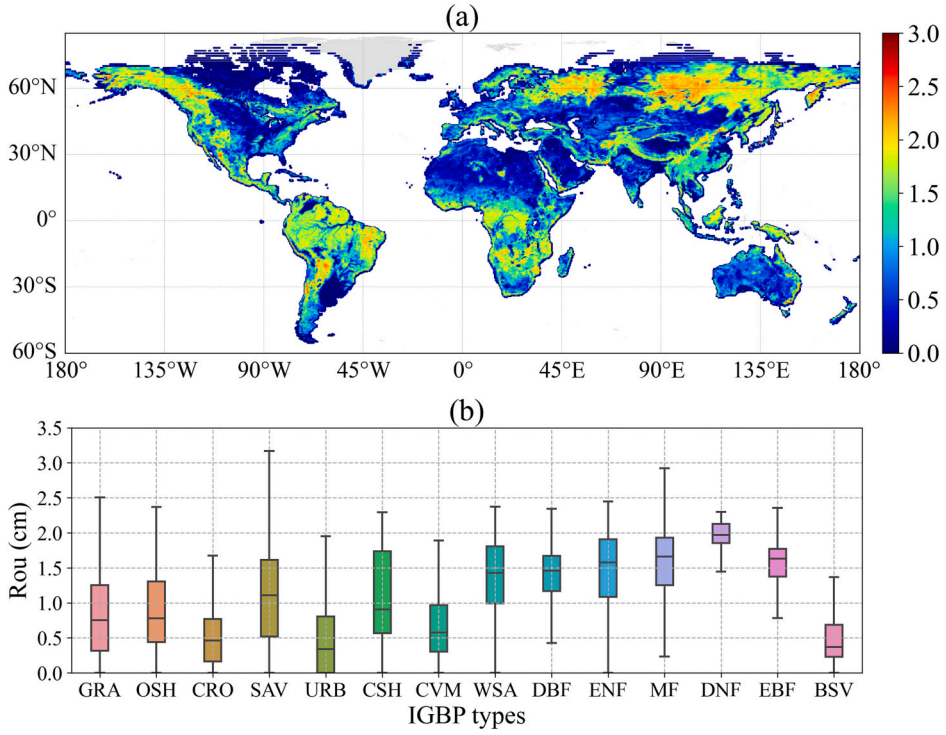

Fig. 3. (a) Spatial distribution, and (b) IGBP-based boxplot of the final *Rou* (s^2/l, unit: cm) obtained by data from 2016 to 2018. The box shows the 25th and 75th percentiles around the median and the whiskers extend to 1.5 times the interquartile range around the percentiles. Abbreviations: GRA (Grasslands), OSH (Open Shrublands), CRO (Croplands), SAV (Savannas), URB (Urban and built-up), CSH (Closed shrubland), CVM (Cropland/natural vegetation mosaics), WSA (Woody savannas), DBF (Deciduous broadleaf forest), ENF (Evergreen needleleaf forest), MF (Mixed forests), DNF (Deciduous needleleaf forest), EBF (Evergreen broadleaf forest), and BSV (Barren).

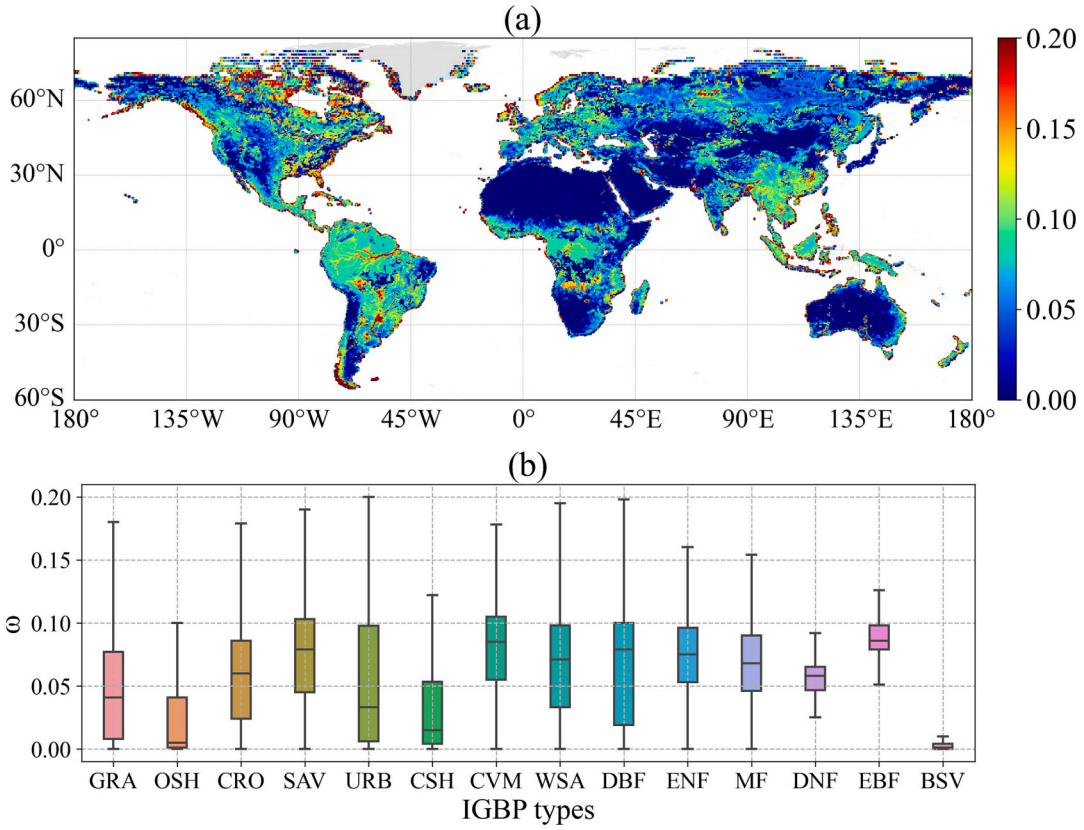

Fig. 4. (a) Spatial distribution, and (b) IGBP-based boxplot of ω obtained by *DoI* using data from 2016 to 2018.

Soil moisture was evaluated with statistical metrics, including Pearson's correlation coefficient (R), bias (m^3/m^3), and ubRMSD (m^3/m^3) (Entekhabi et al., 2010b). The temporal range of SM in the networks is shown in Table 1, with freeze conditions filtered by LST <273.15 K during pre-processing. Given the surface heterogeneity within the SMAP footprint, meter-scale *in-situ* measurements from stations may not precisely represent conditions at the kilometer scale of a pixel. Therefore, for each soil moisture observation dense network, a rectangle boundary was defined using the maximum and minimum longitude and latitude of network stations. The retrieved SM of the pixel within this bounding rectangle was averaged and compared with the network observations. Soil moisture from network observations was computed as the arithmetic average of all stations in the network at the hour closest to the overpass time. For sparse networks such as SCAN, the overall and median values of statistical metrics were calculated for intercomparison across all pixels.

The VOD was evaluated with biomass and canopy height. Because biomass is an annual dataset, the annual averaged VOD (2017 and 2018) was calculated to compare with biomass, and the annual VOD was averaged to compare with canopy heights.

3.4. Sensitivity analysis

The global sensitivity analysis has been widely used to evaluate the uncertainty as described in Razavi et al. (2021), including remotely sensed optical RTM (Chen et al., 2012; Li et al., 2015). A global sensitivity analysis method called high dimensional model representation (HDMR) (Herman and Usher, 2017; Li et al., 2010) was employed to analyze the sensitivity of Tb to SM, VOD, and LST in the MCCA retrieval. Retrieved time-series SM, VOD (H- or V-polarization), and surface temperature (LST) from 2016 to 2018 were set as inputs, and Tb (H- or V-polarization) was set as the output to construct a map of the relationship and analyze the sensitivity of Tb to SM, VOD, and LST over the globe.

4. Results and analysis

4.1. Soil moisture

4.1.1. Spatial patterns of soil moisture

The global spatial pattern of SM is presented in Fig. 5, based on data from 2016 to 2018. The six rows are the results of MCCA, MT-DCA, DCA, SCA-H, SCA-V, and SMAP-IB respectively, while the two columns depict the annual average and seasonal amplitude of SM, respectively. The seasonal amplitude was computed as the annual average of the difference between 95% and 5% percentile of time-series SM after applying a 45-day moving-average filter to the data (Konings et al., 2017; Li et al., 2022).

From the annual average SM, MCCA was found to exhibit a similar spatial pattern to the other algorithms. The lowest SM values were observed in desert areas (*e.g.*, the Sahara, the Taklamakan in the northwest of China, and deserts of Australia, *etc.*). Conversely, the highest SM values were found in dense vegetation areas such as the Amazon and Congo basins. The DCA has higher SM values than other products in the above areas, and South Asia (Fig. 5e). MT-DCA has similar SM values in desert areas but drier SM values in tropical rainforests, and the highest SM appears in boreal forests (Fig. 5c). The dry-wet gradient of MCCA SM is similar to other products, though MCCA was wetter than the other five products in areas of east Brazil, and the western parts of North America. The gradient of SM from the Congo basin to the Sahel of MCCA is rather like that in the MT-DCA than the others, with MCCA and MT-DCA also showing a lower SM gradient than the other algorithms. The difference is most apparent in the boreal forests, with the MCCA and MT-DCA being wetter than other products.

The right column in Fig. 5 shows areas with mid-range SM values that present the highest seasonal amplitude, which aligns with the regions affected by the global monsoon (Fig. 1. in Huang et al. (2020)). In the densely vegetated areas near the equator, the magnitude and dry-wet gradient of the MCCA SM seasonal amplitude is smaller than that of the other products shown in the second column of Fig. 5. SMAP-IB and both of the SCA SM options had higher dry-wet gradients of seasonal amplitude between the tropical forests and non-forest areas than that of the other products.

4.1.2. Validation and inter-comparison of soil moisture products

In this section, the six SM products were compared with the 19 dense SM networks and the SCAN, across various underlying surface and climate zones. The validation statistics are shown in Table 2 and Fig. 6. Overall, all six products had comparable R values (Fig. 6a). The overall items in Table 2 show SMAP-IB had the highest correlation with an R-value of 0.764, followed by DCA (0.753) and MCCA (0.744) in dense networks, which performed slightly better than the other products. For SCAN, both inter-comparison methods show a comparable correlation between all six products. For all six products, R values exceeded 0.6 at most of the networks. All the algorithms performed well for the networks located in the Tibet Plateau except SMN-WDL, where the number of quality-controlled SM values was limited. However, when the quality control procedure of SMAP-IB was discarded and the MT-DCA SM product was excluded, the correlations of the remaining four SM products all exceeded 0.7. The lowest performance in terms of R occurred at the SMN-SDR, installed in the Shandian River Basin of China, with lower R scores compared to those reported by Zheng et al. (2022). This discrepancy was attributed to differences in upscaling methods used for the *in-situ* observations and the application of quality flags. The MySMNet network installed in the tropical forest of Malaysia also exhibited a relatively low R-value, which aligns with findings from Ayres et al. (2021), indicating the challenging nature of accurately estimating SM in forested areas due to the complex structure of forests, litter under the canopy, and signal attenuated by the dense structure of tree trunks and branches.

In dense networks (except TERENO), MCCA, DCA, and SCA-V overestimated the SM with an overall bias of 0.02 m^3/m^3, 0.02 m^3/m^3, 0.014 m^3/m^3, while MT-DCA and SCA-H underestimated SM with a dry bias of 0.014 m^3/m^3, and 0.021 m^3/m^3 respectively, SMAP-IB had the lowest dry bias of 0.006 m^3/m^3. The bias results are consistent with the spatial pattern shown in Fig. 5, and pixel-based validation with a median value in the networks (Li et al., 2022), but different from other evaluation work by Ma et al. (2019).

Table 2 and Fig. 6 indicate that MCCA performed better in terms of ubRMSD over most of these networks (10 over 20), followed by SCA-V with 4 networks. The overall ubRMSD of MCCA (0.055 m^3/m^3) was slightly lower than DCA and SMAP-IB (0.061 m^3/m^3).

Four networks from different continents were selected to visualize the time series performance of the six SM products in Fig. 7. It's observed that MCCA captures the temporal variation, including precipitation events (Fig. 7a), surface thawing in Naqu (Fig. 7c), irrigation (Fig. 7e), and dry-down trends (Fig. 7g), similar to the other five products. All products overestimate SM from July to September 2016, especially SCA-V which hits an upper retrieval limit at the Kyeamba site.

4.2. Polarization-dependent vegetation optical depth

4.2.1. Spatial patterns of vegetation optical depth

Fig. 8 presents the global spatial pattern of VOD based on data from 2016 to 2018. MCCA could retrieve both H- and V-polarized VOD due to the analytical solution of transmissivity, as shown in Fig. 8 (a-d). Because SCA-H and SCA-V algorithms use optical vegetation indices as a proxy of VWC, their VOD is the same as shown in Fig. 8 (i, j). The spatial patterns of annual average VOD of all products exhibited similarities to SM as shown in Fig. 5. Regions characterized by semi-arid conditions tended to have lower VOD values, while tropical forests exhibited the highest VOD values. Among all the products, MT-DCA had the highest

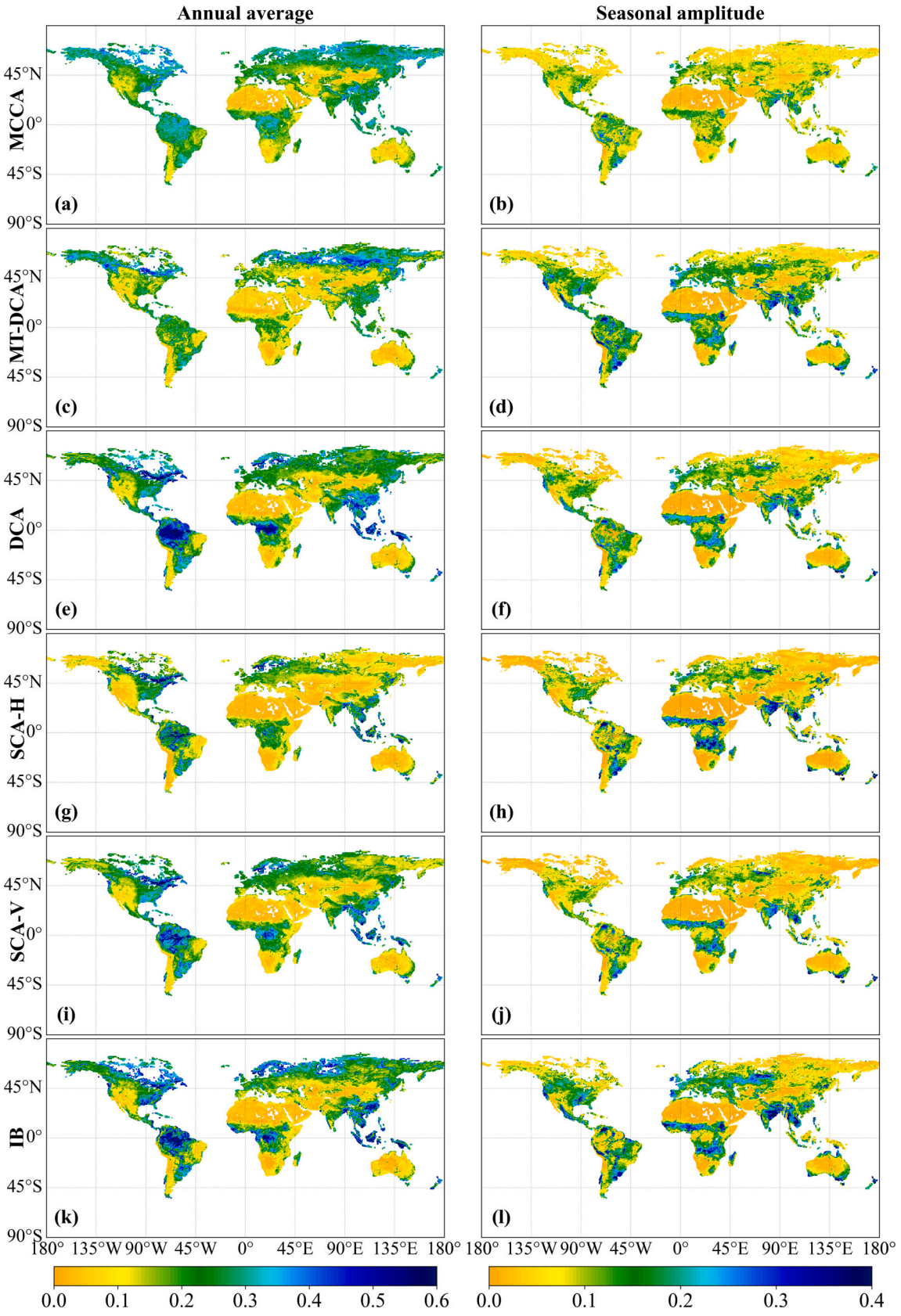

Fig. 5. Global distribution of (left) annual averaged, and (right) mean annual seasonal amplitude (SA) of different SM products from 2016 to 2018, (a-b) MCCA, (c-d) MT-DCA, (e-f) DCA, (g-h) SCA-H, (i-j) SCA-V, and (k-l) SMAP-IB.

Table 2
The network-based validation statistics of different retrieval algorithms with the best performance of the six SM products in each network are marked in bold. Num1 represents the number of samples used for calculating metrics, and Num2 represents the total number of effective retrievals that matched the *in-situ* observations for each product.

Method	Network	R	Bias (m^3/m^3)	ubRMSD (m^3/m^3)	Num1	Num2	Network	R	Bias (m^3/m^3)	ubRMSD (m^3/m^3)	Num1	Num2
MCCA		**0.874**	0.056	**0.026**	564	1179		0.543	0.108	0.045	95	229
MT-DCA		0.854	**0.038**	0.041		1001		**0.630**	**0.018**	**0.038**		186
DCA	Little River	0.861	0.106	0.034		1179	MySMNet	0.627	0.123	0.046		229
SCA-H		0.822	0.081	0.040		1179		0.485	0.143	0.058		229
SCA-V		0.834	0.132	0.032		1179		0.625	0.137	0.048		229
IB		0.846	0.068	0.033		581		0.566	0.102	0.044		96
MCCA		0.865	0.023	0.033	651	1436		0.380	**−0.033**	**0.040**	240	963
MT-DCA		0.885	0.010	0.051		706		0.419	−0.050	0.057		388
DCA	Little Washita	**0.894**	0.008	0.033		1429	SMN-SDR	0.405	−0.051	0.046		641
SCA-H		0.869	−0.050	0.029		1429		0.414	−0.098	0.042		641
SCA-V		0.891	**−0.005**	**0.027**		1429		0.403	−0.062	0.043		641
IB		0.880	−0.009	0.037		666		**0.445**	−0.067	0.042		244
MCCA		0.813	**0.008**	0.045	400	1013		0.583	0.013	**0.026**	44	776
MT-DCA		0.805	−0.029	0.046		728		0.619	−0.064	0.039		157
DCA	Reynolds Creek	0.797	−0.016	0.045		915	SMN-WDL	0.593	0.048	0.049		418
SCA-H		0.773	−0.075	0.049		915		0.610	−0.018	0.043		418
SCA-V		0.793	−0.029	0.047		915		0.613	**0.008**	0.036		418
IB		**0.865**	−0.020	**0.037**		424		**0.632**	0.019	0.030		62
MCCA		0.634	−0.075	0.054	496	1294		0.768	0.074	**0.044**	93	1459
MT-DCA		0.583	−0.089	0.073		783		0.736	**−0.023**	0.058		133
DCA	South Fork	**0.684**	**−0.052**	**0.048**		1136	Maqu	**0.782**	0.076	0.047		1090
SCA-H		0.531	−0.085	0.068		1136		0.718	0.033	0.072		1090
SCA-V		0.633	−0.063	0.054		1136		0.764	0.074	0.060		380
IB		0.601	−0.082	0.063		535		0.739	0.098	0.051		1090
MCCA		0.809	−0.040	0.040	466	1384		**0.894**	0.025	**0.030**	156	1264
MT-DCA		**0.822**	−0.055	0.049		1260		0.887	−0.053	0.041		627
DCA	St. Joseph's	0.821	−0.023	**0.037**		1200	Naqu	0.888	0.065	0.062		883
SCA-H		0.596	−0.034	0.060		1200		0.790	**0.011**	0.082		883
SCA-V		0.755	**−0.015**	0.043		1200		0.835	0.030	0.062		883
IB		0.812	−0.043	0.044		492		0.847	0.026	0.049		220
MCCA		0.844	0.068	0.024	686	1437		0.687	0.055	0.028	200	1052
MT-DCA		0.827	0.039	0.051		766		0.740	0.038	0.039		593
DCA	Walnut Gulch	0.830	0.046	0.031		1435	Pali	0.746	0.054	0.030		833
SCA-H		0.808	−0.020	**0.022**		1435		0.768	−0.098	0.024		833
SCA-V		0.834	0.028	0.023		1435		0.762	−0.030	**0.024**		833
IB		**0.852**	**0.017**	0.032		695		**0.779**	**0.023**	0.029		204
MCCA		0.861	**−0.007**	0.031	631	1431		0.782	0.056	0.020	219	1388
MT-DCA		0.879	−0.021	0.049		706		0.803	**0.003**	0.043		676
DCA	Fort Cobb	**0.886**	−0.015	0.033		1414	Shiquanhe	0.798	0.031	0.034		819
SCA-H		0.860	−0.062	0.033		1414		0.795	−0.057	**0.017**		819
SCA-V		0.881	−0.022	**0.029**		1414		0.800	−0.007	0.019		819
IB		0.885	−0.039	0.035		647		**0.807**	−0.013	0.032		224
MCCA		0.850	0.037	**0.044**	568	1179		0.839	0.019	**0.036**	882	1795
MT-DCA		0.860	0.020	0.069		1013		**0.850**	**0.000**	0.054		1418
DCA	Kyeamba	0.866	0.040	0.058		1179	TERENO	0.804	0.005	0.043		1771
SCA-H		0.859	0.030	0.089		1179		0.714	−0.052	0.046		1771
SCA-V		0.870	0.050	0.074		1179		0.736	−0.006	0.045		1771
IB		**0.881**	**0.002**	0.060		578		nan	nan	nan	0	0
MCCA		0.846	0.061	**0.044**	571	1187		0.744	0.020	**0.055**	7574	22,223
MT-DCA		0.862	0.033	0.075		1016	Overall of dense networks except TERENO	0.684	−0.014	0.071		13,896
DCA	Yanco	0.868	0.052	0.056		1187		0.753	0.020	0.061		19,447
SCA-H		0.874	**0.027**	0.076		1187		0.706	−0.021	0.073		19,447
SCA-V		0.878	0.055	0.065		1187		0.711	0.014	0.067		19,447
IB		**0.881**	0.028	0.066		583		**0.764**	**−0.006**	0.061		8160
MCCA		0.795	0.016	**0.032**	714	1429		0.688	0.008	0.055	86,864	125,161
MT-DCA		0.817	−0.010	0.054		1413		0.688	−0.025	0.061		109,255
DCA	REMEDHUS	0.836	**−0.001**	0.038		1429	Median of SCAN	0.707	0.003	0.054		111,104
SCA-H		0.818	−0.029	0.041		1429		0.660	−0.042	0.058		111,106
SCA-V		0.827	−0.006	0.040		1429		0.693	−0.001	**0.052**		111,106
IB		**0.841**	−0.014	0.047		723		**0.719**	**0.000**	0.056		93,167

(*continued on next page*)

Table 2 (*continued*)

Method	Network	R	Bias (m^3/m^3)	ubRMSD (m^3/m^3)	Num1	Num2	Network	R	Bias (m^3/m^3)	ubRMSD (m^3/m^3)	Num1	Num2
MCCA		0.729	0.018	**0.044**	780	2123		0.721	**0.007**	0.086	86,864	125,161
MT-DCA		0.757	−0.089	0.050		1744		0.607	−0.033	0.104		109,255
DCA	HOBE	0.771	0.027	0.052		2031	Overall of SCAN	0.740	0.010	**0.085**		111,104
SCA-H		0.677	**−0.002**	0.052		2031		0.735	−0.033	0.090		111,106
SCA-V		0.753	0.024	0.049		2031		**0.743**	0.008	0.086		111,106
IB		**0.822**	−0.021	0.050		806		0.737	0.007	0.097		93,167

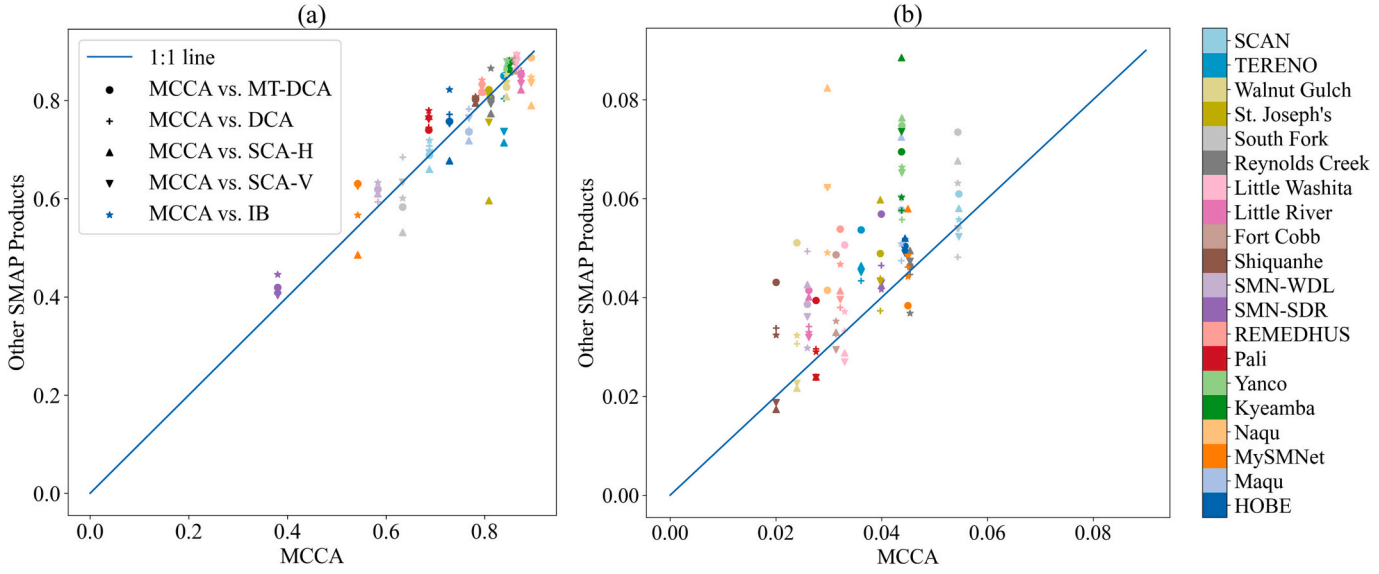

Fig. 6. The network-based (a) R and (b) ubRMSD (unit: m^3/m^3) from Table 2.

VOD in densely vegetated areas (Fig. 8e), while the spatial gradient of VOD for MCCA was comparable to that of the other products across the globe. In arid areas such as central Asia, and northwest China, DCA and SCA exhibited almost zero values, indicating little to no vegetation. In contrast, MCCA, MT-DCA, and SMAP-IB showed a presence of vegetation in these regions based on their VOD values.

Regarding the seasonal amplitude of VOD, all six products exhibited a similar spatial pattern in most areas of the globe. For example, North America showed a lower seasonal cycle in the west compared to the east, while central and western Asia exhibited a smaller amplitude than that of the periphery of Asia. DCA and SCA generally show higher amplitude than the other products in areas with a high seasonal cycle. The main difference in seasonal amplitude is observed in forested areas and transitional zones between forests and non-forests, particularly in the Amazon and Congo regions. In the Amazon, both the MCCA and MT-DCA VOD products exhibited a seasonal cycle, while the DCA and SMAP-IB had low seasonal amplitude except in areas close to streams of the Amazon River (Fig. 8h, l). However, this seasonal cycle was not observed in SCA (Fig. 8j). This discrepancy in seasonal amplitude arises because DCA and SCA use the NDVI climatology to initialize the retrieval or to directly calculate VOD, respectively (O'Neill et al., 2021a). However, a saturation effect occurs for NDVI values higher than 0.7–0.8 (Rodríguez-Fernández et al., 2018) due to the strong absorption in the red wavelength (Tian et al., 2016). Additionally, excessive regularization may have been applied in the DCA VOD retrievals (Chaparro et al., 2022), which makes the resulting VOD closely related to the prior input of the NDVI climatology. Therefore, the VOD of DCA and SCA shows less variability compared to that of MCCA and MT-DCA, which do not rely on auxiliary data in the retrieval process. Around the Congo basin, including the Sahel and south Congo, both MCCA VODs exhibit analogous spatial patterns to DCA, SCA, and SMAP-IB products, with the highest amplitude observed in MCCA products. However, no obvious gradient features are observed in MT-DCA (Fig. 8f). More detailed time series variations of VODs are shown and analyzed in Fig. S2 in the supplementary material.

Fig. 9 presents the relationship between polarization-dependent VODs retrieved by MCCA after the retrieval spikes were removed. The VOD values between H- and V-polarization exhibit a strong correlation globally, except for arid areas like the Saraha desert where H-polarized VOD remains close to zero (Fig. 9a). The polarization-dependent VODs provide more information compared to polarization-independent VOD, as indicated by DoI > 1) (Fig. 9b). While the annual average difference between H- and V-polarized VOD is not prominent in most areas, difference can be observed in tropical forests, the Sahara, southern Saudi Arabia, central Australia, and fragment areas in Asia (Fig. 9c). Generally, the H-polarized VOD was ~0.015 higher than the V-polarized VOD in densely vegetated areas, while the V-polarized VOD was ~0.03 higher than the H-polarized VOD in the Sahara. Further discussion is provided in Section 5.3.

4.2.2. *Relationship with aboveground biomass and canopy height*

Fig. 10 presents a comparison of the six VOD products with the ESA-CCI AGB from 2017 to 2018 (unit: Mg ha^{-1}) (Santoro and Cartus, 2023) and GEDI-based canopy height (Dubayah et al., 2020; Dubayah et al., 2021). It was found that all six products exhibited a strong linear relationship with biomass and canopy height. Notably, the canopy is semi-transparent to the L-band, which in turn is more sensitive to the tree's vertical structure. Additionally, the small leaves of the tree are essentially transparent. It is logical that VOD would have a more pronounced linear relationship with tree height, whereas foliage affects AGB but not

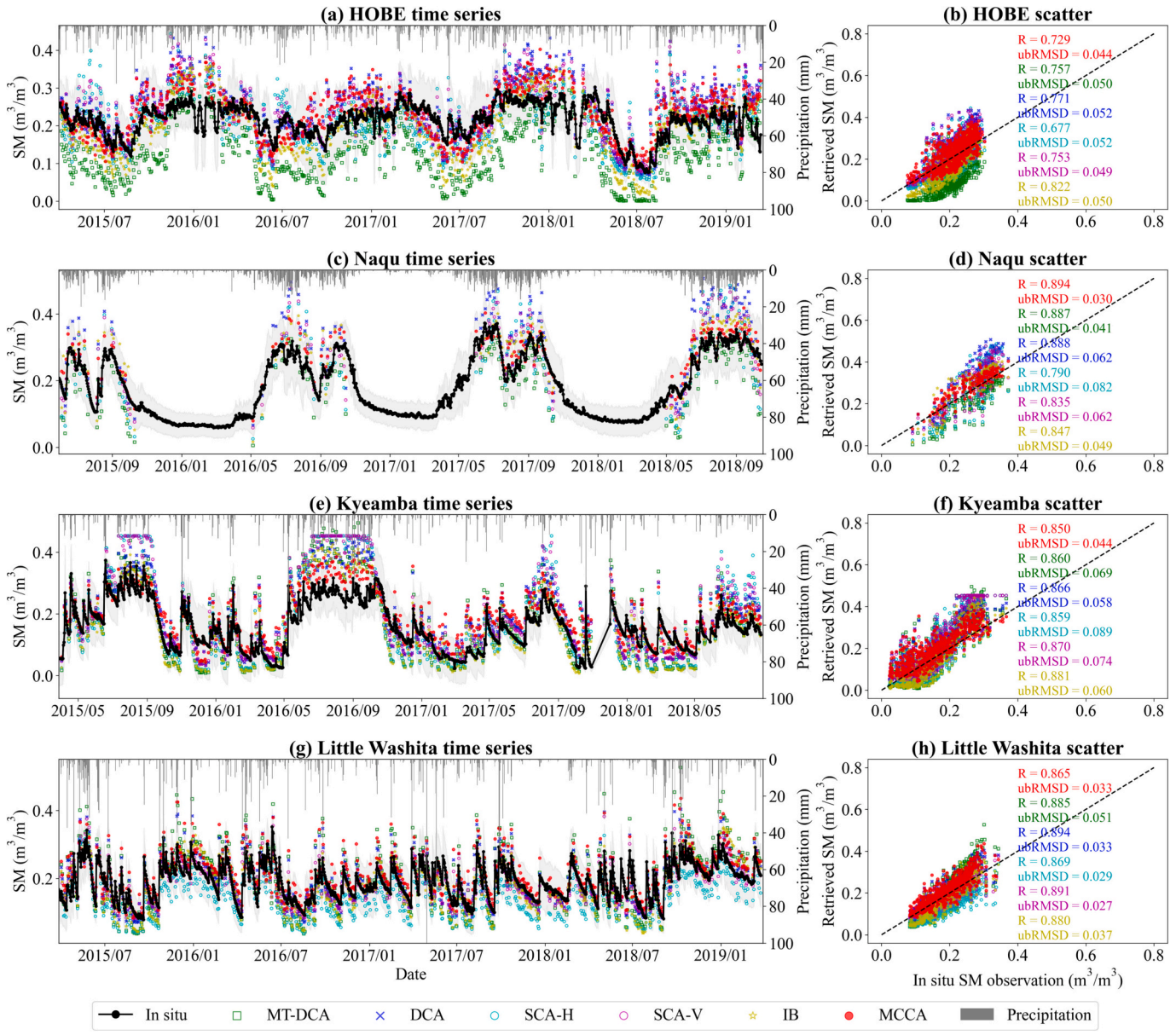

Fig. 7. Time series and scatter plots of the six SM products with the period listed in Table 1 at (a-b) HOBE (Denmark), (c-d) Naqu (China), (e-f) Kyeamba (Australia), and (g-h) Little Washita (USA), respectively. Time series plots contain daily precipitation (mm/day) shown in the axis on the right side (grey bar). Note that daily precipitation accumulates liquid and frozen water, including rain and snow.

canopy height. The relationships between MCCA VOD at both V- and H-polarizations and biomass/canopy height are similar to those of MT-DCA and SMAP-IB. The relationship between SCA (DCA) and biomass and canopy height have a sharp increment around VOD of 1.25 (Fig. 10d, e, j, k) as expected since they are not retrieved but directly computed from NDVI. These findings about MT-DCA, DCA, and SCA are consistent with the SMAP-IB algorithm discussed in Li et al. (2022). Overall, Fig. 10 offers valuable information about the spatial relationships between VOD, biomass, and canopy height. However, for a comprehensive understanding of these relationships over time, further investigation and analysis considering the temporal dynamics of VWC and environmental conditions are necessary.

5. Discussion

5.1. Global sensitivity analysis of MCCA

Fig. 11 maps the global sensitivity analysis results of MCCA at dual-polarization using a HDMR approach. The analysis was conducted based on the retrieved results from 2016 to 2018, and the least robust pixels (total sensitivity indices <0.9 or >1.1) were masked as blank. This analysis revealed that different areas have different dominant factors influencing the Tb at H- and V-polarization in the MCCA. For H-polarization (Fig. 11a), SM had the highest sensitivity to Tb in arid areas such as the northern Sahel, deserts in Australia, and the Gobi in Mongolia. In the western parts of the Americas and Asia, both SM and surface temperature (LST) contribute substantially to Tb variations, as indicated by the purple color. In densely vegetated areas, the sensitivity of Tb at H-polarization was found to be higher in boreal forests compared to tropical forests. In the transition zones between dense and sparse vegetated areas, the dominant factors were SM and VOD (colored in teal), such as in the savanna climate areas around the Amazon, Congo basin, and India. In Southeast China, the sensitivity of Tb to LST was higher than that of SM and VOD. In summary, the sensitivity of Tb at H-polarization to these three variables exhibited distinct regional features.

Regarding the result of Tb at V-polarization (Fig. 11b), the sensitivity

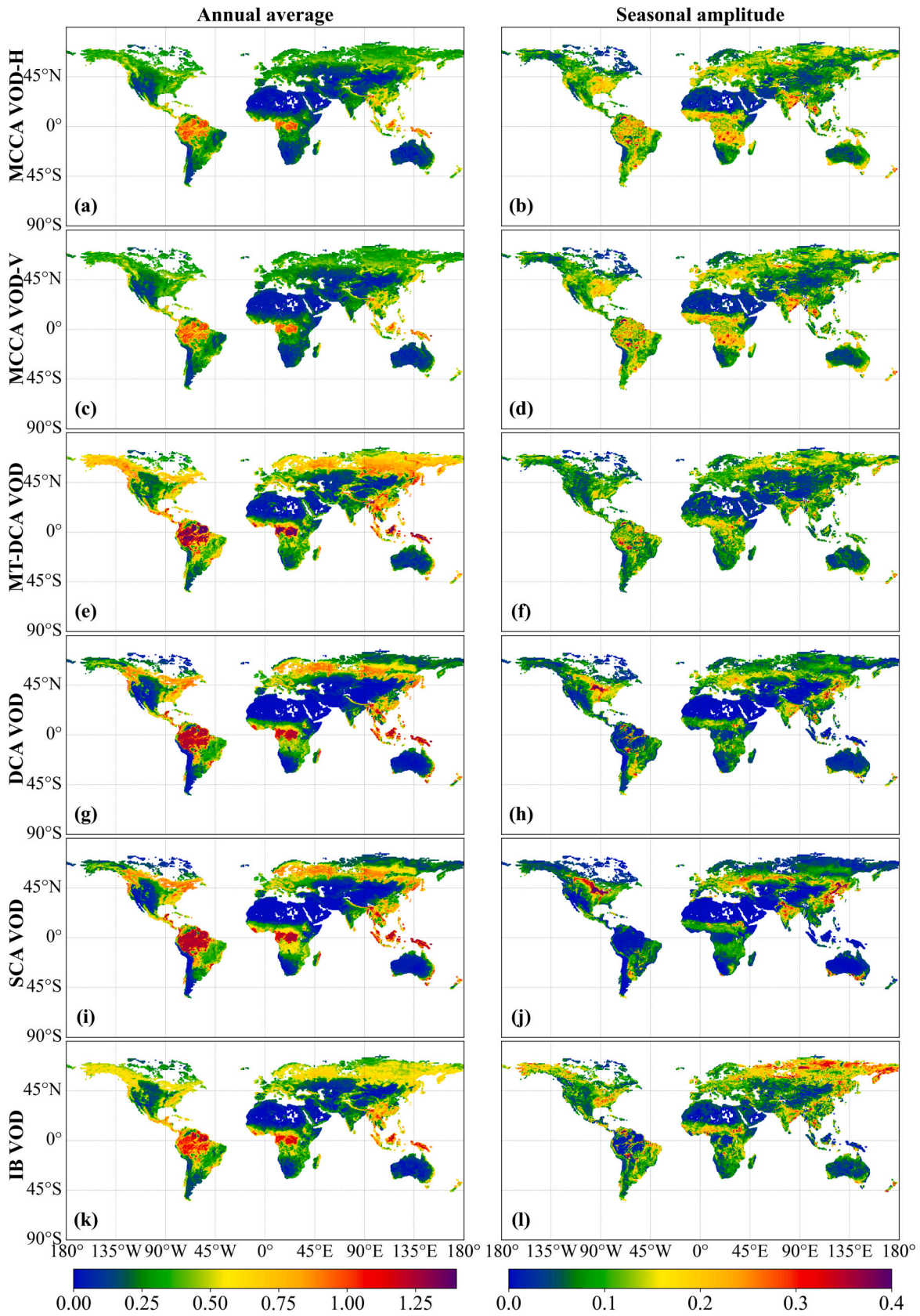

Fig. 8. Global distribution of annual averaged (left column), and mean annual seasonal amplitude (right column) of different VOD products from 2016 to 2018, (a-b) MCCA VOD-H, (c-d) MCCA VOD-V, (e-f) MT-DCA, (g-h) DCA, (i-j) SCA, and (k-l) SMAP-IB.

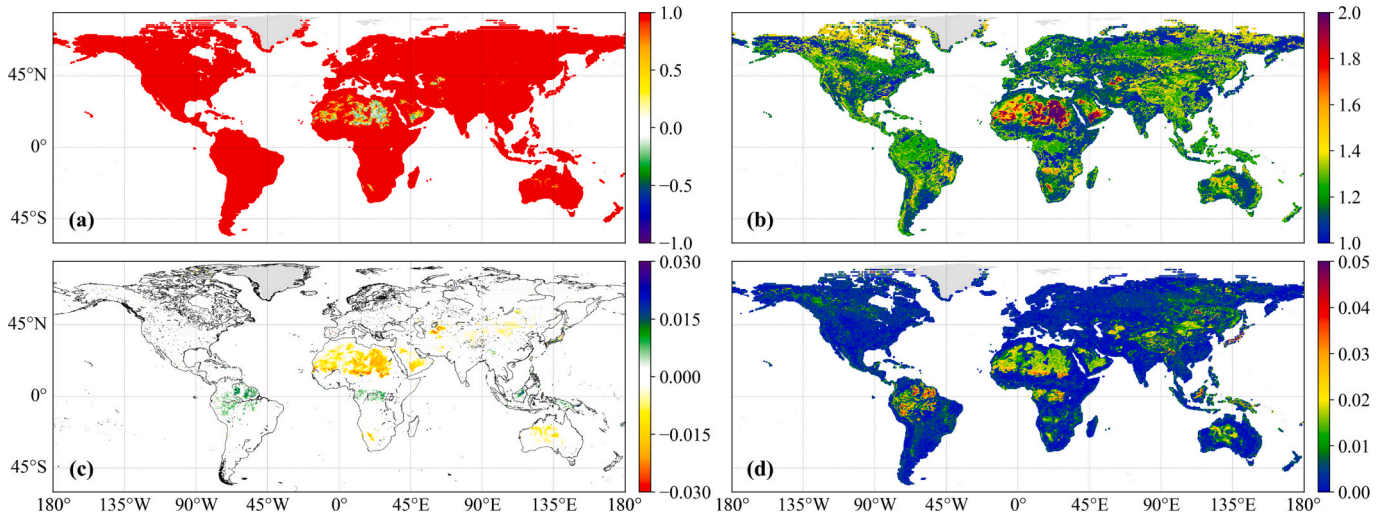

Fig. 9. Global distribution of polarization-dependent VOD (2016–2018) characteristics: (a) correlation coefficient between 7-day moving average H- and V-polarized VODs, (b) DoI between H- and V-polarized VODs, (c) annual averaged difference (H-polarization minus V-polarization), and (d) annual average seasonal amplitude of difference. Grey pixels indicate no valid data.

of SM and LST dominated most areas globally, except for the boreal forest (where VOD and LST were dominant) and the ocean-continent boundaries. This suggests that the VOD of the boreal forest exhibits significant annual dynamics. A decrease in VOD may potentially be linked to freezing in the boreal forest (Schwank et al., 2021). The area dominated by SM at V-polarized Tb was larger compared to that of H-polarization in Fig. 11a. Notably, many studies have found that Tb at H-polarization is more sensitive to SM at L-band, but using the one-factor-at-a-time (or step-wise) approach (Balsamo et al., 2006; Hornbuckle and England, 2004). However, when considering multiple factors, including LST, and vegetation effects, the dominance of SM influencing V-polarized Tb is greater than that of H-polarized Tb. This finding is consistent with the SMAP team's previous use of SCA-V as the baseline SM retrieval algorithm (O'Neill et al., 2020), which generally outperforms the SCA-H.

In the tropical rainforest areas near the equator, both H- and V-polarized Tbs exhibited higher sensitivity to SM and LST. This indicates that changes in Tb in these areas are primarily driven by variations in SM and LST, suggesting that the L-band microwave frequencies have a certain capability to retrieve SM even under the dense vegetation cover, such as in the Amazon and Congo basin. Conversely, the low sensitivity of VOD in these tropical densely vegetated areas may indicate that VOD tends to remain relatively stable, and its impact on Tb is weaker compared to changes in SM and LST. This finding is consistent with the results obtained from the SCA and DCA algorithms (see Fig. S3 in Supplementary material). However, it is important to note that MT-DCA shows higher sensitivity to SM in these areas compared to other algorithms, as indicated in Fig. S3.

5.2. Uncertainty and variability of vegetation optical depth

The MCCA retrieved VOD values are relatively smaller compared to other products, which corresponds to different model parameters leading to different estimates of vegetation or roughness effects. This discrepancy in VOD can be partially attributed to the variation in effective roughness values used by different retrieval algorithms. For example, SCA has a roughness parameter (Hp) ranging from 0 to 0.16, MT-DCA uses a fixed global value of 0.13, DCA has a Hp range from 0 to approximately 2 (excluding areas heavily influenced by terrain, with a median of 0.56), and *Rou* in MCCA ranges from 0 to 3 (excluding areas heavily influenced by terrain, with a median of 0.79). Similarly, a recent study found that seasonal variation in VOD retrievals for dense tropical forests is strongly affected by constant omega values (Wang et al., 2023). Therefore, VOD and roughness parameters are more like conceptual variables as they are both effective values under the framework of the τ-ω model. It can be therefore very challenging to obtain their physical magnitudes (Frappart et al., 2020; Njoku and Chan, 2006; Wang et al., 2021; Wigneron et al., 2017). Additionally, the roughness parameter, originally defined as a geometric roughness, is sensitive to surface dielectric properties (Bai et al., 2022; Peng et al., 2017; Schneeberger et al., 2004; Schwank et al., 2010; Wigneron et al., 2017; Wigneron et al., 2001). High emissivity (manifested as low dielectric constant) due to the presence of litter has been observed in ground experiments over forest and grass regions (Grant et al., 2008; Grant et al., 2007; Guglielmetti et al., 2008; Saleh et al., 2006; Schwank et al., 2008) and in satellite retrievals from SMOS and AMSR (Karthikeyan et al., 2019; Parrens et al., 2016). Consequently, the surface roughness can be influenced by the presence of litter and the dynamic processes of litter interception, which can result in a rough dielectric interface and thus affect the VOD retrieval.

Fig. 12 shows the global distribution of R between MCCA VOD at H-polarization and other products (the result calculated by VOD at V-polarization is in Fig. S4 in the supplementary material). The results indicate that there is a high correlation between MCCA and MT-DCA, DCA, and SMAP-IB VOD over most of the globe, particularly for DCA VOD. MT-DCA and SMAP-IB showed comparable correlations with MCCA in terms of trend, while SMAP-IB had a higher correlation with MCCA in terms of anomalies. It's noteworthy that although DCA VOD exhibited lower seasonal amplitude in the tropical forests as shown in Fig. 8(h) and Fig. S2(c), the anomalies of MCCA VOD are highly correlated with DCA VOD (Fig. 12d). As mentioned in Fig. S2, it seems that MCCA had different oscillation with other products, which can be attributed to two features. First, MCCA utilized the relationship between SM and VOD of the core channel to derive the Tb at the collaborative channels. Second, the VOD calculation in MCCA was based on an analytical solution. Other algorithms (except SCA) employ multi-temporal (MT-DCA) or Tikhonov regularization (DCA, SMAP-IB) to minimize the solution space in their iterative procedure. The balance between smoothing and capturing short-time variability of VOD is challenging for regularization (Chaparro et al., 2022).

5.3. Vegetation optical depth at dual polarization

Section 4.2 indicates that there is a polarization difference in VOD at

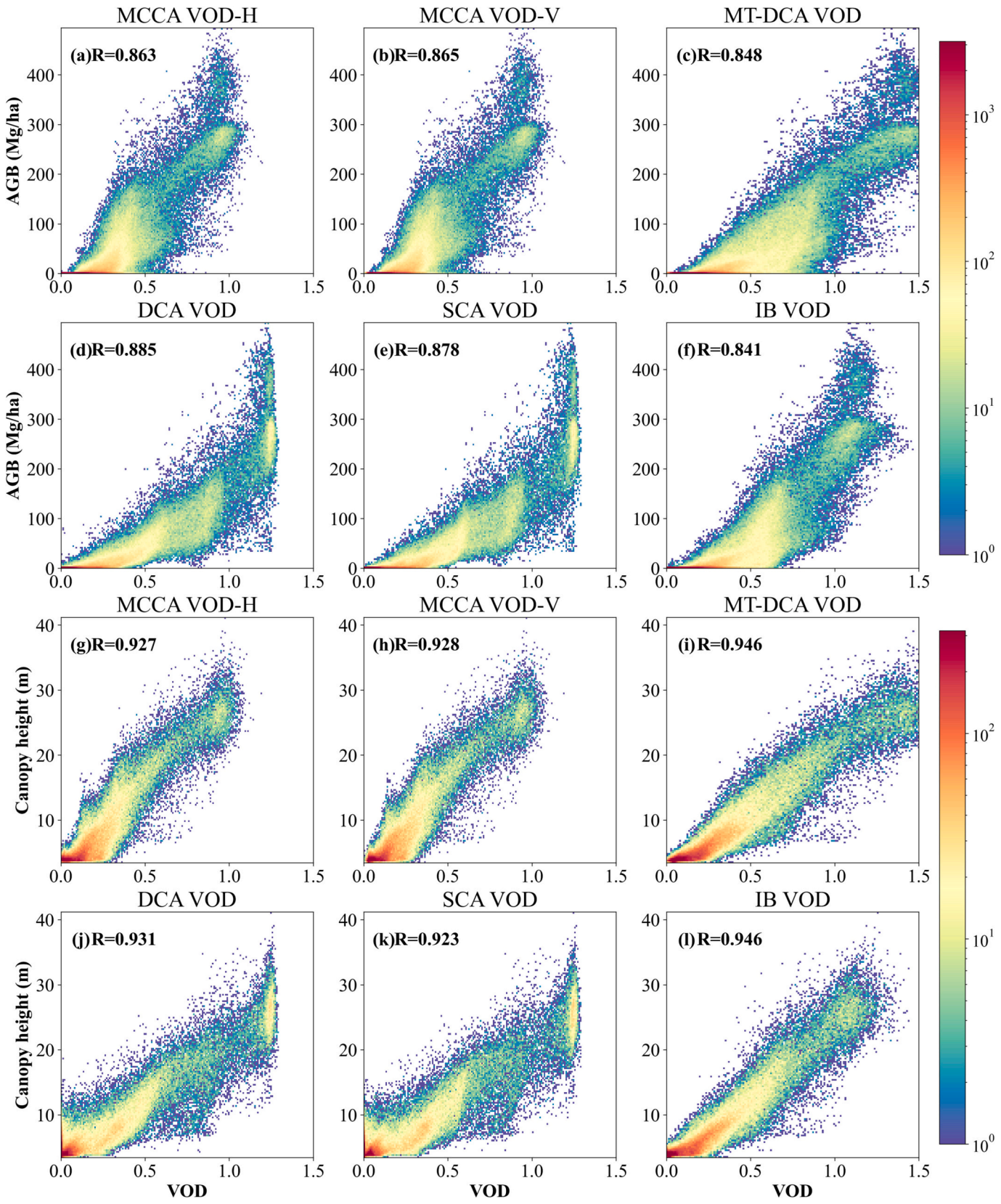

Fig. 10. Density scatter plots of the six VOD products (annually averaged) against AGB, in Mg ha^{-1} (first two rows), canopy height (the last two rows), and the color-bars are in the log10 scale.

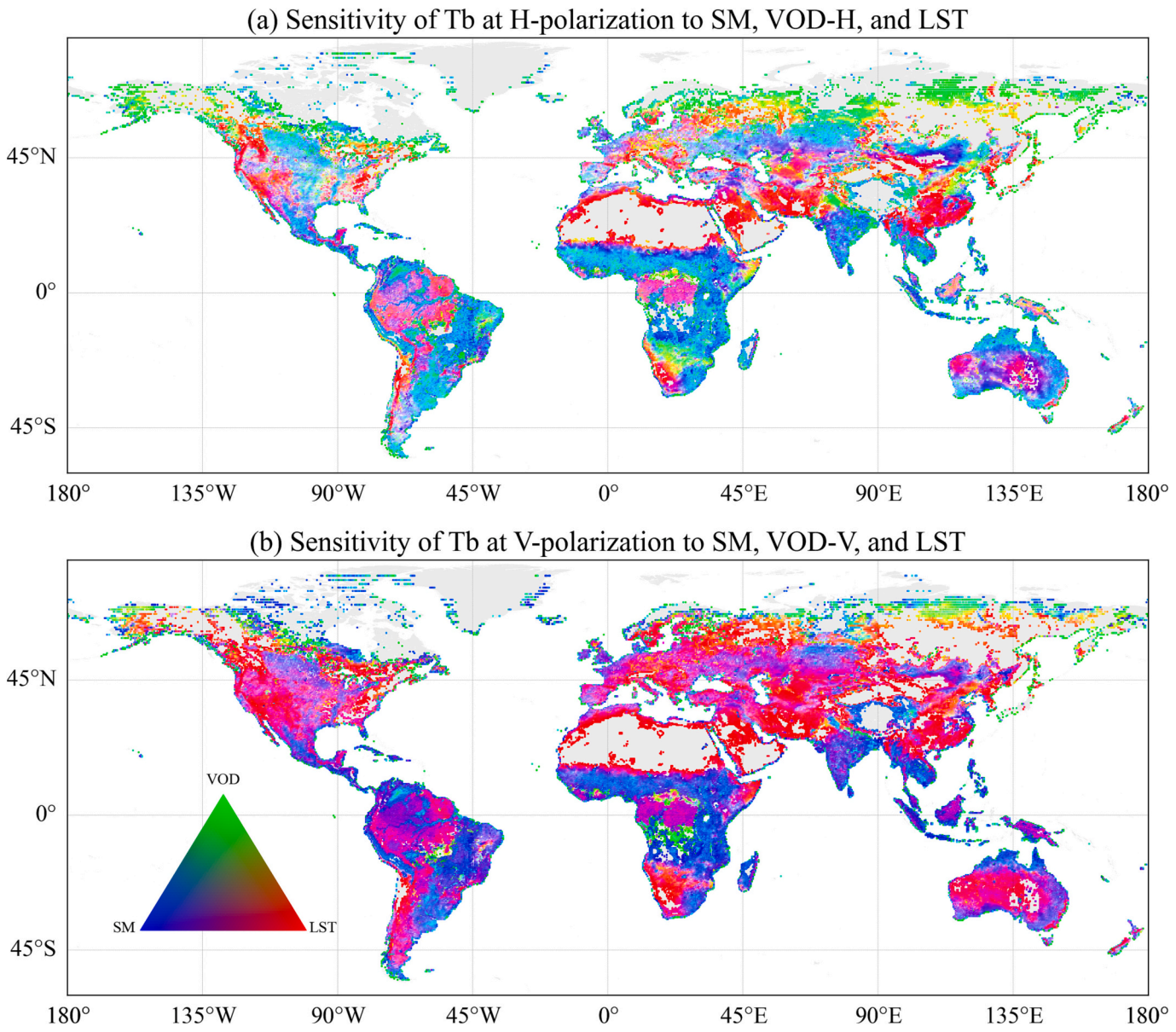

Fig. 11. Map of the global sensitivity analysis result of MCCA at (a) H-polarization, and (b) V-polarization. The sensitivity of LST, VOD (H/V), and SM to Tb (H/V) was used to construct the depth of red, green, and blue maps. For example, if the sensitivity of SM in HDMR is the highest at a pixel, it is colored blue; if the sensitivity of SM and LST are about equal with a small sensitivity of VOD, it is colored purple. (For interpretation of the references to color in this figure legend, the reader is referred to the web version of this article.)

the satellite scale, with the differences in VOD polarization in this study mainly located in tropical rainforests and arid areas (Fig. 9). Fig. 13 presents boxplots comparing the different SM and VOD products in two representative regions: the Sahara and an equatorial area. The figure highlights that the major difference between the products is observed in VOD rather than SM. In the Sahara region (Fig. 13a, b), varying ranges of VOD were observed among different products. DCA and SCA VOD values were zero in most of the Sahara due to the utilization of NDVI climatology and land cover type (parameter b is set as 0 in barren) in their calculation. MT-DCA and SMAP-IB exhibited small VOD values but not zero. MCCA VODs show distinct differences: MCCA VOD-H resembles SCA and DCA with values close to zero, while MCCA VOD-V resembles MT-DCA and SMAP-IB with a median value <0.04. It is noteworthy that recent research has indicated that more than one-quarter of Africa's tree cover is outside areas previously classified as forest, extending even to the Sahara desert (Fig. 14a-b) (Reiner et al., 2023b). MCCA, MT-DCA, and SMAP-IB aligned well with the distribution of tree coverage in the Saraha, as shown in the right column of Fig. 14. and the fact that plants like ferns still occur today in the Tibesti mountains (of the Sahara) for supporting animals (Runge et al., 2022). However, further investigation is needed to explore vegetation distribution in the Sahara, especially since there is no valid tree coverage for the central Sahara region. Moreover, the Sahara vegetation exhibited higher V-polarized VOD (Fig. 14e) compared to H-polarized VOD (Fig. 14c), a phenomenon that requires additional research to understand its implications.

The observed difference between VOD at H- and V-polarization in the densely vegetated area can be attributed to the impact of the canopy structure on the microwave radiation transfer process (Ulaby et al., 1987; Wigneron et al., 1995). Canopy structure, which is affected by factors such as vertical stalks in forests, plays a significant role in this regard. This finding aligns with the result of previous studies conducted on forested experiments, such as the research by Grant et al. (2008). Additionally, recent advancements in polarized VOD estimation based on multi-angular SMOS observations and alternative algorithms that

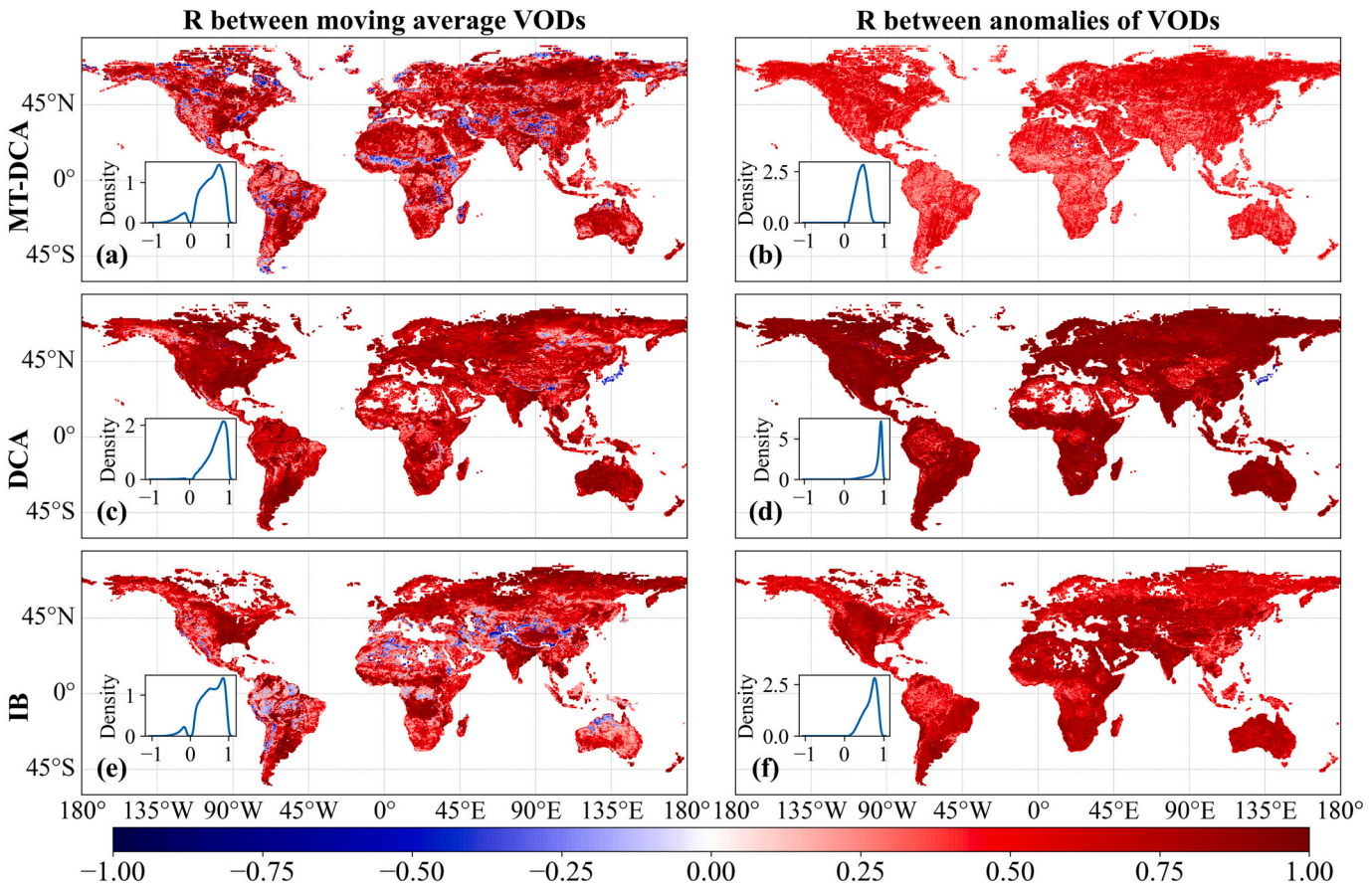

Fig. 12. Map of R between MCCA calculated VOD at H-polarization and other products (2016–2018). The left column is calculated by the 7-day moving average result, and the right column is calculated by the corresponding anomalies (VOD minus the 7-day moving average VOD). The blank pixels correspond to p values >0.05. No inter-mask is applied here.

incorporate microwave vegetation indices have also corroborated these findings (Bai et al., 2022).

Fig. 15 illustrates density plots showcasing the relationship between VOD and AGB, along with canopy height for both H- and V- polarizations. These plots are based on the SMOS retrieval using the multi-temporal and multi-angular (MTMA) algorithm (Bai et al., 2022). Notably, the polarization difference of VOD is more pronounced in SMOS, resulting in significantly greater disparities between H- and V-polarization, AGB, and canopy height compared to the polarized VOD retrieved by MCCA from SMAP observations. The advantage of MCCA is that polarization-dependent VOD can be retrieved from limited SMAP observations. However, it requires the assumption that the vegetation omega is the same for both V- and H -polarization, resulting in uncertainties in VOD retrieval. In contrast, the MTMA utilizes SMOS multi-angular information to independently derive the vegetation albedo and VOD for V- and H- polarization. Thus, it is expected that the SMOS-derived VOD should be more reasonable. However, algorithms that utilize multi-angular information may have significant uncertainties when vegetation is dense due to a weak angle dependence of microwave emission. Consequently, differences in VOD performance with AGB and canopy height between SMOS and SMAP result from differences between the multi-angular and dual-polarization algorithms.

It's important to note that, although SMOS theoretically provides more information with its multi-angular observations, the polarized VOD of MCCA in SMAP exhibits a stronger correlation with AGB and canopy height (Fig. 15). As there are currently only two products with polarization-dependent VOD, it is challenging to conclude which algorithm performs "better" in the retrieval of VOD. It is expected to implement the MCCA to SMOS data thus creating a physically consistent SMOS and SMAP polarization-dependent VOD. Based on the presented results and analysis, it is confirmed that there exists a polarization difference in VOD at the satellite scale, which is not only caused by the retrieval algorithm.

6. Conclusion

This study introduced a novel parameter self-calibrating framework for the MCCA algorithm as a new approach for retrieving SM and polarization-dependent VOD using the dual-polarized Tb observations at the fixed incidence angle (40°) from the SMAP mission. The whole MCCA algorithm offers two key features:

(1) The new parameter self-calibrating framework uses information-based technology to obtain surface parameters including ω and surface roughness at a global scale without the need for ancillary data.

(2) This method enables the retrieval of VOD with polarization differences simultaneously with SM. It is particularly challenging because SMAP only has two channels (dual-polarized Tb observations at a fixed incidence angle).

To assess the performance of the retrieved SM and VOD, comparisons were conducted with five other SMAP-based algorithms, namely MT-DCA, DCA, SCA-H, SCA-V, and SMAP-IB. The evaluation of SM involved *in-situ* observations from 19 dense and 1 sparse soil moisture network. Given the challenge of comparing VOD with *in-situ* measurements, the polarization-dependent VODs were assessed using ESA-CCI AGB and GEDI-based canopy height.

Based on the statistical metrics obtained from the network-based comparison, no algorithm demonstrated an absolute advantage over the others. Among the dense networks, SMAP-IB achieved the highest

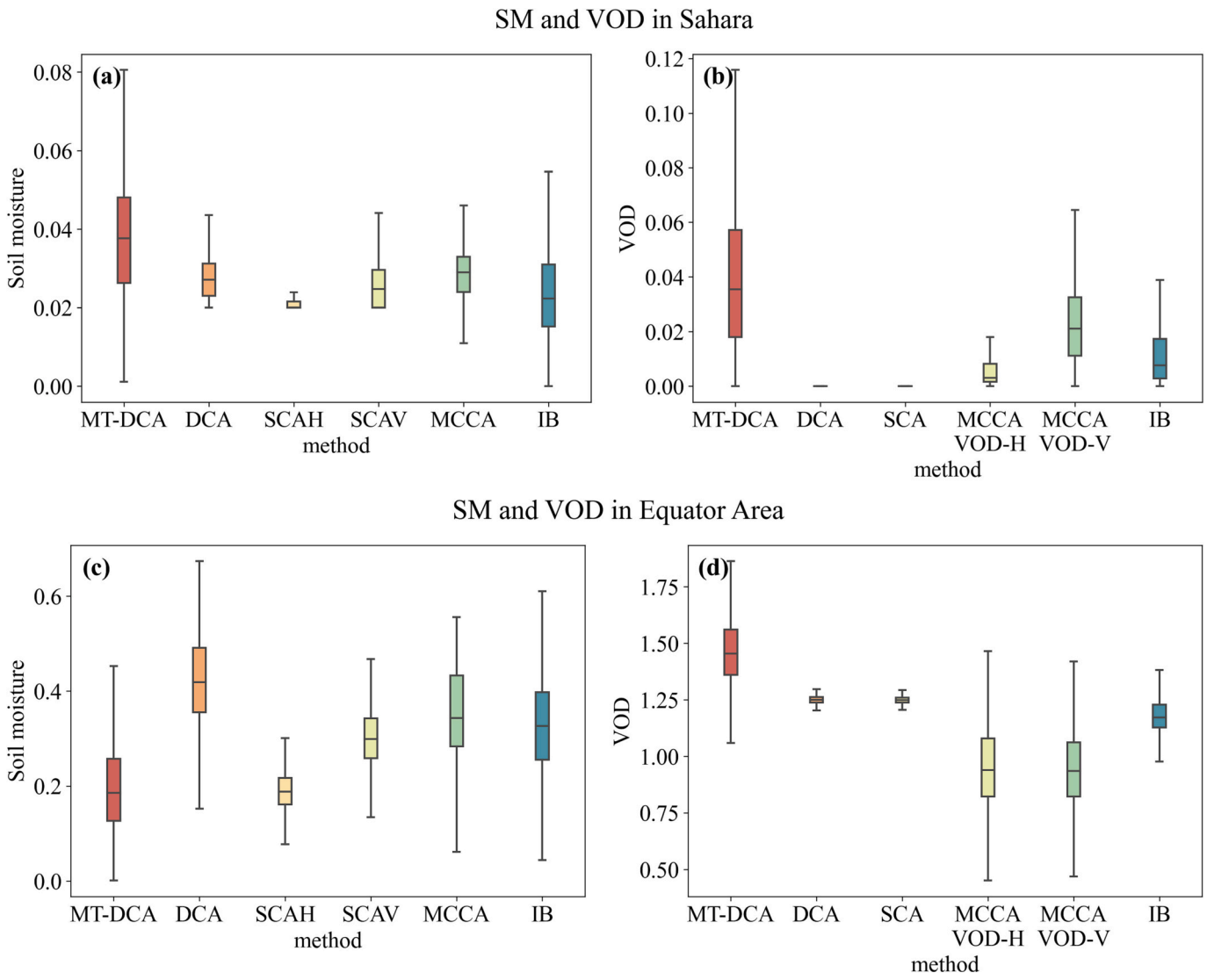

Fig. 13. Boxplot of the six SM and VOD products from 2016 to 2018 at (a-b) Sahara (latitudes range: 15° to 35°, longitudes range: −20° to 60°) and (c-d) Equatorial (latitudes range: −12° to 10°, longitudes range: −80° to 150°) areas. The box shows the 25th and 75th percentiles while the whiskers extend to 1.5 times the interquartile range around the median.

overall R score of 0.764, followed by DCA (0.753) and MCCA (0.744). Regarding ubRMSD, MCCA exhibited the lowest value (0.055 m^3/m^3), followed closely by the SMAP-IB and DCA (0.061 m^3/m^3). Similar levels of accuracy were observed in the sparse network SCAN. The spatial pattern of different SM products exhibited similarities and differences.

Both H- and V-polarized VOD retrieved by the MCCA exhibited analogous spatial patterns to VOD from other products. Arid areas generally exhibited low VOD values, while densely vegetated areas showed high VOD values. The trend (7-day moving average) and corresponding anomalies of MCCA VOD had the highest correlation with DCA, while MT-DCA and SMAP-IB VOD showed a comparable correlation with MCCA in terms of trend. SMAP-IB has a higher correlation of anomalies with MCCA compared to MT-DCA. All six VOD products demonstrated strong linearity with AGB and canopy height.

The MCCA retrieved results revealed a slight difference in the polarization-dependent VODs depending on the specific vegetation characteristics at the satellite scale while maintaining a high degree of correlation. The findings indicated higher H-polarized VOD in densely vegetated areas and higher V-polarized VOD in arid areas. The methodology employed in this study enhanced SMAP's capability to retrieve polarized VOD, thus expanding its potential applications. The polarization-dependent VOD provides additional information and offers an opportunity to deepen understanding of the water transport in the soil-vegetation-atmosphere. By combining the polarization-dependent VODs at L-band (SMAP) and together with the VODs at different frequencies of AMSR (Hu et al., 2023), it should be possible to observe the vegetation hydraulic properties (Konings et al., 2021).

CRediT authorship contribution statement

Zhiqing Peng: Conceptualization, Data curation, Formal analysis, Investigation, Methodology, Software, Validation, Visualization, Writing – original draft, Writing – review & editing. **Tianjie Zhao:** Conceptualization, Investigation, Methodology, Visualization, Writing – original draft, Writing – review & editing. **Jiancheng Shi:** Conceptualization, Funding acquisition, Project administration, Resources. **Lu Hu:** Data curation, Formal analysis, Investigation, Software. **Nemesio J. Rodríguez-Fernández:** Formal analysis, Writing – review & editing. **Jean-Pierre Wigneron:** Formal analysis, Writing – review & editing. **Thomas J. Jackson:** Formal analysis, Writing – review & editing. **Jeffrey P. Walker:** Formal analysis, Writing – review & editing. **Michael H. Cosh:** Data curation, Writing – review & editing. **Kun Yang:** Writing

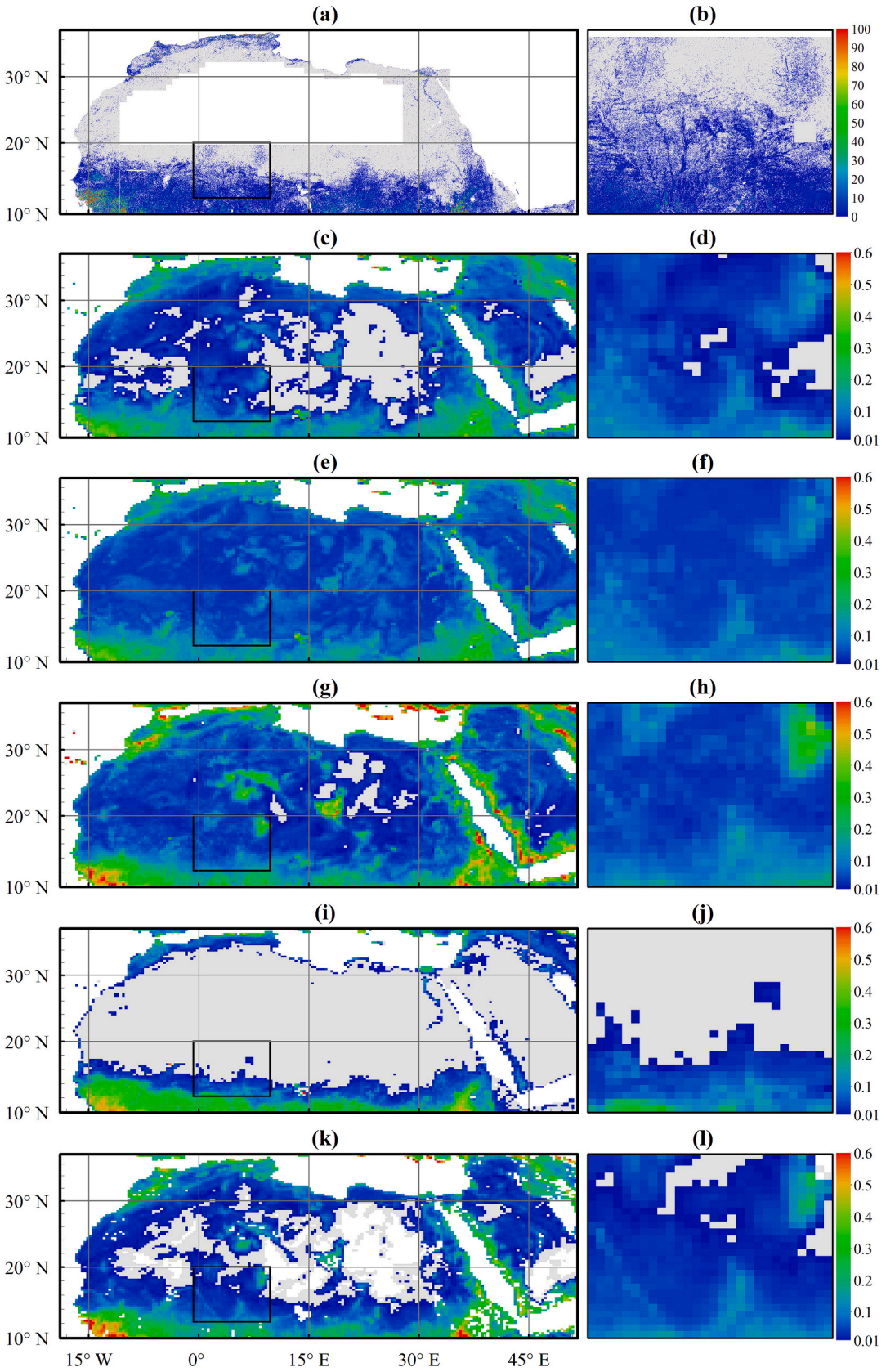

Fig. 14. Spatial distribution of tree coverage (a-b) and average VODs (c-l) from five VOD products (2016 to 2018): (c-d) MCCA VOD-H, (e-f) MCCA VOD-V, (g-h) MT-DCA, (i-j) DCA, and (k-l) SMAP-IB. The right columns show detailed views of the selected area indicated by the black box in the left column. Grey pixels represent areas with average VOD values below 0.01, while white pixels indicate regions with no valid data. No inter-mask is applied here.

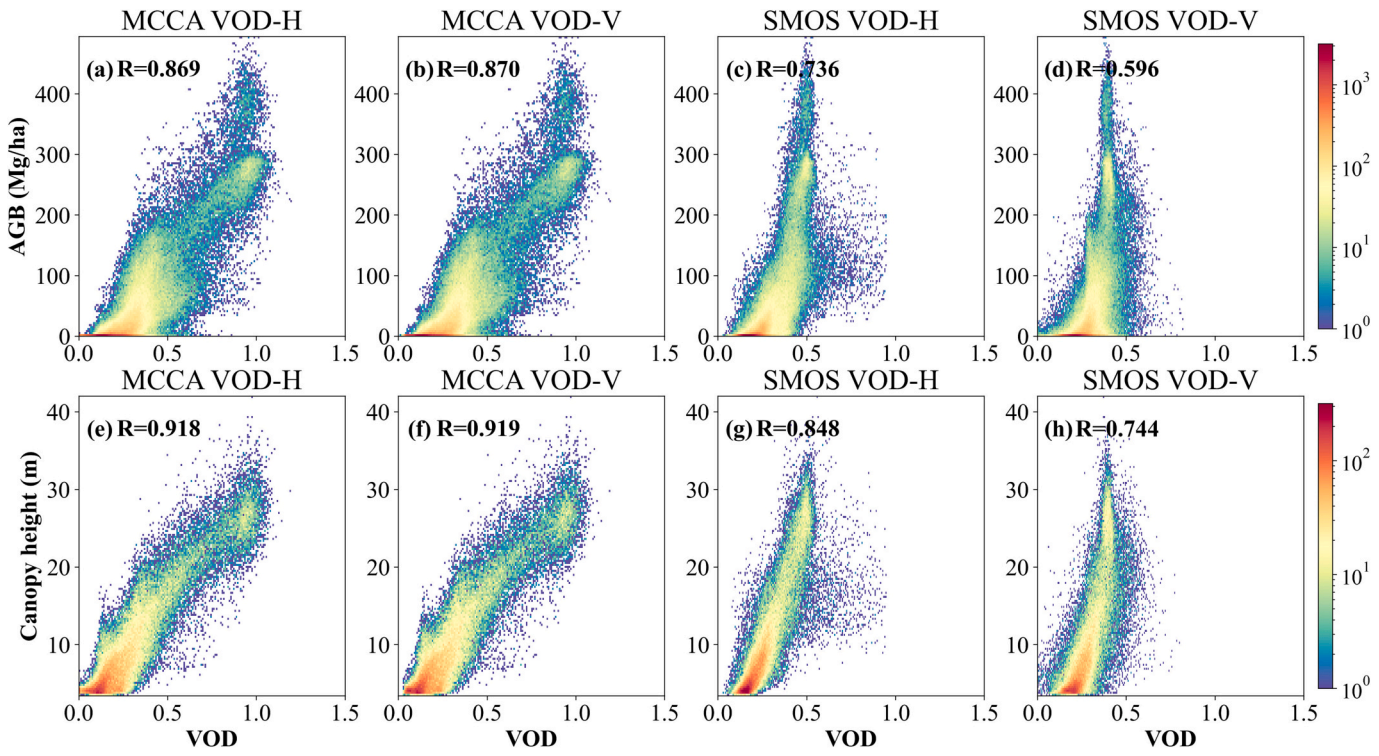

Fig. 15. Same as Fig. 10, but AGB and canopy height compared with the polarized VOD products: (a-b) and (e-f) SMAP, (c-d) and (g-h) SMOS. The R-values for SMAP differ from those in Fig. 10 because this figure represents an inter-mask of SMAP and SMOS.

– review & editing. **Hui Lu:** Writing – review & editing. **Yu Bai:** Data curation, Formal analysis. **Panpan Yao:** Data curation. **Jingyao Zheng:** Formal analysis. **Zushuai Wei:** Formal analysis.

Declaration of Competing Interest

The authors declare that they have no known competing financial interests or personal relationships that could have appeared to influence the work reported in this paper.

Data availability

The SMAP SM and VOD product using MCCA was developed by the Aerospace Information Research Institute, Chinese Academy of Sciences, with the data available at the National Tibetan Plateau/Third Pole Environment Data Center (https://doi.org/10.11888/Terre.tpdc.272088). The SMAP INRAE-Bordeaux (IB) VOD data set is available at https://ib.remote-sensing.inrae.fr/.

Acknowledgements

This study was jointly supported by the National Key Research and Development Program of China (No. 2022YFB3903302) and the National Natural Science Foundation of China (No. 42090014). Nemesio J. Rodríguez-Fernández was partially supported by the CNES TOSCA project SMOS-HR and the Dragon V project (No. 59312). This research was supported in part by the U.S. Department of Agriculture, Agricultural Research Service. USDA is an equal opportunity provider and employer. This research was a contribution from the USDA Long-Term Agroecosystem Research (LTAR) network. We thank the reviewers and Prof. Brian K. Hornbuckle for comments that improved the paper.

Appendix A. Supplementary data

Supplementary data to this article can be found online at https://doi.org/10.1016/j.rse.2023.113970.

References

Adnan, S., Maltamo, M., Mehtätalo, L., Ammaturo, R.N.L., Packalen, P., Valbuena, R., 2021. Determining maximum entropy in 3D remote sensing height distributions and using it to improve aboveground biomass modelling via stratification. Remote Sens. Environ. 260, 112464.

Arjovsky, M., Chintala, S., Bottou, L., 2017. Wasserstein generative adversarial networks. In: Doina, P., Yee Whye, T. (Eds.), Proceedings of the 34th International Conference on Machine Learning, pp. 214–223. Proceedings of Machine Learning Research: PMLR.

Ayres, E., Colliander, A., Cosh, M.H., Roberti, J.A., Simkin, S., Genazzio, M.A., 2021. Validation of SMAP soil moisture at terrestrial National Ecological Observatory Network (NEON) sites show potential for soil moisture retrieval in forested areas. IEEE J. Select. Top. Appl. Earth Observ. Remote Sens. 14, 10903–10918.

Bai, Y., Zhao, T., Jia, L., Cosh, M.H., Shi, J., Peng, Z., Li, X., Wigneron, J.-P., 2022. A multi-temporal and multi-angular approach for systematically retrieving soil moisture and vegetation optical depth from SMOS data. Remote Sens. Environ. 280, 113190.

Balsamo, G., Mahfouf, J.F., Bélair, S., Deblonde, G., 2006. A global root-zone soil moisture analysis using simulated L-band brightness temperature in preparation for the hydros satellite mission. J. Hydrometeorol. 7, 1126–1146.

Bastiaanssen, W.G.M., Menenti, M., Feddes, R.A., Holtslag, A.A.M., 1998. A remote sensing surface energy balance algorithm for land (SEBAL). 1. Formulation. J. Hydrol. 212–213, 198–212.

Baur, M.J., Jagdhuber, T., Feldman, A.F., Akbar, R., Entekhabi, D., 2019. Estimation of relative canopy absorption and scattering at L-, C- and X-bands. Remote Sens. Environ. 233, 111384.

Baur, M.J., Jagdhuber, T., Feldman, A.F., Chaparro, D., Piles, M., Entekhabi, D., 2021. Time-variations of zeroth-order vegetation absorption and scattering at L-band. Remote Sens. Environ. 267, 112726.

Brunfeldt, D.R., Ulaby, F.T., 1984. Measured microwave emission and scattering in vegetation canopies. IEEE Trans. Geosci. Remote Sens. GE-22, 520–524.

Chan, S.K., Bindlish, R., O'Neill, P., Jackson, T., Njoku, E., Dunbar, S., Chaubell, J., Piepmeier, J., Yueh, S., Entekhabi, D., Colliander, A., Chen, F., Cosh, M.H., Caldwell, T., Walker, J., Berg, A., McNairn, H., Thibeault, M., Martínez-Fernández, J., Uldall, F., Seyfried, M., Bosch, D., Starks, P., Holifield Collins, C., Prueger, J., van der Velde, R., Asanuma, J., Palecki, M., Small, E.E., Zreda, M., Calvet, J., Crow, W.T., Kerr, Y., 2018. Development and assessment of the SMAP enhanced passive soil moisture product. Remote Sens. Environ. 204, 931–941.

Chaparro, D., Feldman, A.F., Chaubell, M.J., Yueh, S.H., Entekhabi, D., 2022. Robustness of vegetation optical depth retrievals based on L-band global radiometry. IEEE Trans. Geosci. Remote Sens. 60, 1–17.

Chaubell, M.J., Yueh, S.H., Dunbar, R.S., Colliander, A., Chen, F., Chan, S.K., Entekhabi, D., Bindlish, R., O'Neill, P.E., Asanuma, J., Berg, A.A., Bosch, D.D., Caldwell, T., Cosh, M.H., Collins, C.H., Martínez-Fernández, J., Seyfried, M., Starks, P.J., Su, Z., Thibeault, M., Walker, J., 2020. Improved SMAP dual-channel algorithm for the retrieval of soil moisture. IEEE Trans. Geosci. Remote Sens. 58, 3894–3905.

Chen, L., Yan, G., Wang, T., Ren, H., Calbó, J., Zhao, J., McKenzie, R., 2012. Estimation of surface shortwave radiation components under all sky conditions: modeling and sensitivity analysis. Remote Sens. Environ. 123, 457–469.

Cover, T.M., Thomas, J.A., 2005. Entropy, relative entropy, and mutual information. In: Elements of Information Theory, pp. 13–55.

Dorigo, W.A., Wagner, W., Hohensinn, R., Hahn, S., Paulik, C., Xaver, A., Gruber, A., Drusch, M., Mecklenburg, S., van Oevelen, P., Robock, A., Jackson, T., 2011. The International Soil Moisture Network: a data hosting facility for global in situ soil moisture measurements. Hydrol. Earth Syst. Sci. 15, 1675–1698.

Dubayah, R., Blair, J.B., Goetz, S., Fatoyinbo, L., Hansen, M., Healey, S., Hofton, M., Hurtt, G., Kellner, J., Luthcke, S., Armston, J., Tang, H., Duncanson, L., Hancock, S., Jantz, P., Marselis, S., Patterson, P.L., Qi, W., Silva, C., 2020. The Global Ecosystem Dynamics Investigation: high-resolution laser ranging of the Earth's forests and topography. Sci. Remote Sens. 1, 100002.

Dubayah, R.O., Luthcke, S.B., Sabaka, T.J., Nicholas, J.B., Preaux, S., Hofton, M.A., 2021. GEDI L3 Gridded Land Surface Metrics, Version 2. ORNL Distributed Active Archive Center.

Ebtehaj, A., Bras, R.L., 2019. A physically constrained inversion for high-resolution passive microwave retrieval of soil moisture and vegetation water content in L-band. Remote Sens. Environ. 233, 111346.

Entekhabi, D., Njoku, E.G., Neill, P.E.O., Kellogg, K.H., Crow, W.T., Edelstein, W.N., Entin, J.K., Goodman, S.D., Jackson, T.J., Johnson, J., Kimball, J., Piepmeier, J.R., Koster, R.D., Martin, N., McDonald, K.C., Moghaddam, M., Moran, S., Reichle, R., Shi, J.C., Spencer, M.W., Thurman, S.W., Tsang, L., Zyl, J.V., 2010a. The Soil Moisture Active Passive (SMAP) mission. Proc. IEEE 98, 704–716.

Entekhabi, D., Reichle, R.H., Koster, R.D., Crow, W.T., 2010b. Performance metrics for soil moisture retrievals and application requirements. J. Hydrometeorol. 11, 832–840.

Fan, L., Wigneron, J.-P., Ciais, P., Chave, J., Brandt, M., Fensholt, R., Saatchi, S.S., Bastos, A., Al-Yaari, A., Hufkens, K., Qin, Y., Xiao, X., Chen, C., Myneni, R.B., Fernandez-Moran, R., Mialon, A., Rodriguez-Fernandez, N.J., Kerr, Y., Tian, F., Peñuelas, J., 2019. Satellite-observed pantropical carbon dynamics. Nat. Plants 5, 944–951.

Feldman, A., Konings, A., Piles, M., Entekhabi, D., 2021a. The Multi-Temporal Dual Channel Algorithm (MT-DCA). Zenodo.

Feldman, A.F., Chaparro, D., Entekhabi, D., 2021b. Error propagation in microwave soil moisture and vegetation optical depth retrievals. IEEE J. Select. Top. Appl. Earth Observ. Remote Sens. 14, 11311–11323.

Frappart, F., Wigneron, J.-P., Li, X., Liu, X., Al-Yaari, A., Fan, L., Wang, M., Moisy, C., Le Masson, E., Aoulad Lafkih, Z., Vallé, C., Ygorra, B., Baghdadi, N., 2020. Global monitoring of the vegetation dynamics from the vegetation optical depth (VOD): a review. Remote Sens. 12.

Gao, L., Sadeghi, M., Ebtehaj, A., 2020a. Microwave retrievals of soil moisture and vegetation optical depth with improved resolution using a combined constrained inversion algorithm: application for SMAP satellite. Remote Sens. Environ. 239, 111662.

Gao, L., Sadeghi, M., Feldman, A.F., Ebtehaj, A., 2020b. A spatially constrained multichannel algorithm for inversion of a first-order microwave emission model at L-band. IEEE Trans. Geosci. Remote Sens. 58, 8134–8146.

Gao, L., Ebtehaj, A., Chaubell, M.J., Sadeghi, M., Li, X., Wigneron, J.-P., 2021. Reappraisal of SMAP inversion algorithms for soil moisture and vegetation optical depth. Remote Sens. Environ. 264, 112627.

GCOS-138, 2010. Implementation Plan for the Global Observing System for Climate in Support of the UNFCCC - 2010 Update. World Meteorological Organization.

Grant, J.P., Wigneron, J.P., Van de Griend, A.A., Kruszewski, A., Søbjærg, S.S., Skou, N., 2007. A field experiment on microwave forest radiometry: L-band signal behaviour for varying conditions of surface wetness. Remote Sens. Environ. 109, 10–19.

Grant, J.P., Saleh-Contell, K., Wigneron, J., Guglielmetti, M., Kerr, Y.H., Schwank, M., Skou, N., Griend, A.A.V.d., 2008. Calibration of the L-MEB model over a coniferous and a deciduous forest. IEEE Trans. Geosci. Remote Sens. 46, 808–818.

Green, J.K., Seneviratne, S.I., Berg, A.M., Findell, K.L., Hagemann, S., Lawrence, D.M., Gentine, P., 2019. Large influence of soil moisture on long-term terrestrial carbon uptake. Nature 565, 476–479.

Guglielmetti, M., Schwank, M., Matzler, C., Oberdorster, C., Vanderborght, J., Fluhler, H., 2008. FOSMEX: forest soil moisture experiments with microwave radiometry. IEEE Trans. Geosci. Remote Sens. 46, 727–735.

Gulrajani, I., Ahmed, F., Arjovsky, M., Dumoulin, V., Courville, A., 2017. Improved training of wasserstein GANs. In: Proceedings of the 31st International Conference on Neural Information Processing Systems. Curran Associates Inc., Long Beach, California, USA, pp. 5769–5779.

Hengl, T., Mendes de Jesus, J., Heuvelink, G.B.M., Ruiperez Gonzalez, M., Kilibarda, M., Blagotić, A., Shangguan, W., Wright, M.N., Geng, X., Bauer-Marschallinger, B., Guevara, M.A., Vargas, R., MacMillan, R.A., Batjes, N.H., Leenaars, J.G.B., Ribeiro, E., Wheeler, I., Mantel, S., Kempen, B., 2017. SoilGrids250m: global gridded soil information based on machine learning. PLoS One 12, e0169748.

Herman, J., Usher, W., 2017. SALib: an open-source Python library for sensitivity analysis. J. Open Source Softw. 2, 97.

Hornbuckle, B.K., England, A.W., 2004. Radiometric sensitivity to soil moisture at 1.4 GHz through a corn crop at maximum biomass. Water Resour. Res. 40.

Hornbuckle, B.K., Patton, J.C., VanLoocke, A., Suyker, A.E., Roby, M.C., Walker, V.A., Iyer, E.R., Herzmann, D.E., Endacott, E.A., 2016. SMOS optical thickness changes in response to the growth and development of crops, crop management, and weather. Remote Sens. Environ. 180, 320–333.

Hu, L., Zhao, T., Ju, W., Peng, Z., Shi, J., Rodríguez-Fernández, N.J., Wigneron, J.-P., Cosh, M.H., Yang, K., Lu, H., Yao, P., 2023. A twenty-year dataset of soil moisture and vegetation optical depth from AMSR-E/2 measurements using the multi-channel collaborative algorithm. Remote Sens. Environ. 292, 113595.

Huang, E., Wang, P., Wang, Y., Yan, M., Tian, J., Li, S., Ma, W., 2020. Dole effect as a measurement of the low-latitude hydrological cycle over the past 800 ka. Sci. Adv. 6, eaba4823.

Jackson, T.J., 1993. III. Measuring surface soil moisture using passive microwave remote sensing. Hydrol. Process. 7, 139–152.

Jackson, T.J., Schmugge, T.J., 1991. Vegetation effects on the microwave emission of soils. Remote Sens. Environ. 36 (3), 1991. 203–200.

Jackson, T.J., Bindlish, R., Cosh, M.H., Zhao, T., Starks, P.J., Bosch, D.D., Seyfried, M., Moran, M.S., Goodrich, D.C., Kerr, Y.H., Leroux, D., 2012. Validation of Soil Moisture and Ocean Salinity (SMOS) soil moisture over watershed networks in the U. S. IEEE Trans. Geosci. Remote Sens. 50, 1530–1543.

Karthikeyan, L., Pan, M., Wanders, N., Kumar, D.N., Wood, E.F., 2017. Four decades of microwave satellite soil moisture observations: Part 1. A review of retrieval algorithms. Adv. Water Resour. 109, 106–120.

Karthikeyan, L., Pan, M., Konings, A.G., Piles, M., Fernandez-Moran, R., Nagesh Kumar, D., Wood, E.F., 2019. Simultaneous retrieval of global scale Vegetation Optical Depth, surface roughness, and soil moisture using X-band AMSR-E observations. Remote Sens. Environ. 234, 111473.

Kerr, Y.H., Waldteufel, P., Wigneron, J., Delwart, S., Cabot, F., Boutin, J., Escorihuela, M., Font, J., Reul, N., Gruhier, C., Juglea, S.E., Drinkwater, M.R., Hahne, A., Martin-Neira, M., Mecklenburg, S., 2010. The SMOS mission: new tool for monitoring key elements ofthe global water cycle. Proc. IEEE 98, 666–687.

Kerr, Y.H., Waldteufel, P., Richaume, P., Wigneron, J.P., Ferrazzoli, P., Mahmoodi, A., Bitar, A.A., Cabot, F., Gruhier, C., Juglea, S.E., Leroux, D., Mialon, A., Delwart, S., 2012. The SMOS soil moisture retrieval algorithm. IEEE Trans. Geosci. Remote Sens. 50, 1384–1403.

Konings, A.G., McColl, K.A., Piles, M., Entekhabi, D., 2015. How many parameters can be maximally estimated from a set of measurements? IEEE Geosci. Remote Sens. Lett. 12, 1081–1085.

Konings, A.G., Piles, M., Rötzer, K., McColl, K.A., Chan, S.K., Entekhabi, D., 2016. Vegetation optical depth and scattering albedo retrieval using time series of dual-polarized L-band radiometer observations. Remote Sens. Environ. 172, 178–189.

Konings, A.G., Piles, M., Das, N., Entekhabi, D., 2017. L-band vegetation optical depth and effective scattering albedo estimation from SMAP. Remote Sens. Environ. 198, 460–470.

Konings, A.G., Saatchi, S.S., Frankenberg, C., Keller, M., Leshyk, V., Anderegg, W.R.L., Humphrey, V., Matheny, A.M., Trugman, A., Sack, L., Agee, E., Barnes, M.L., Binks, O., Cawse-Nicholson, K., Christoffersen, B.O., Entekhabi, D., Gentine, P., Holtzman, N.M., Katul, G.G., Liu, Y., Longo, M., Martinez-Vilalta, J., McDowell, N., Meir, P., Mencuccini, M., Mrad, A., Novick, K.A., Oliveira, R.S., Siqueira, P., Steele-Dunne, S.C., Thompson, D.R., Wang, Y., Wehr, R., Wood, J.D., Xu, X., Zuidema, P.A., 2021. Detecting forest response to droughts with global observations of vegetation water content. Glob. Chang. Biol. 27, 6005–6024.

Kornelsen, K.C., Coulibaly, P., 2015. Design of an Optimal Soil Moisture Monitoring Network using SMOS retrieved soil moisture. IEEE Trans. Geosci. Remote Sens. 53, 3950–3959.

Kurum, M., 2013. Quantifying scattering albedo in microwave emission of vegetated terrain. Remote Sens. Environ. 129, 66–74.

Li, G., Rabitz, H., Yelvington, P.E., Oluwole, O.O., Bacon, F., Kolb, C.E., Schoendorf, J., 2010. Global sensitivity analysis for systems with independent and/or correlated inputs. Chem. Eur. J. 114, 6022–6032.

Li, L., Xin, X., Zhang, H., Yu, J., Liu, Q., Yu, S., Wen, J., 2015. A method for estimating hourly photosynthetically active radiation (PAR) in China by combining geostationary and polar-orbiting satellite data. Remote Sens. Environ. 165, 14–26.

Li, X., Wigneron, J.-P., Fan, L., Frappart, F., Yueh, S.H., Colliander, A., Ebtehaj, A., Gao, L., Fernandez-Moran, R., Liu, X., Wang, M., Ma, H., Moisy, C., Ciais, P., 2022. A new SMAP soil moisture and vegetation optical depth product (SMAP-IB): algorithm, assessment and inter-comparison. Remote Sens. Environ. 271, 112921.

Liu, Y.Y., van Dijk, A.I.J.M., de Jeu, R.A.M., Canadell, J.G., McCabe, M.F., Evans, J.P., Wang, G., 2015. Recent reversal in loss of global terrestrial biomass. Nat. Clim. Chang. 5, 470–474.

Lu, H., Koike, T., Fujii, H., Ohta, T., Tamagawa, K., 2009. Development of a physically-based soil moisture retrieval algorithm for spaceborne passive microwave radiometers and its application to AMSR-E. J. Remote Sens. Soc. Jpn. 29, 253–262.

Ma, H., Zeng, J., Chen, N., Zhang, X., Cosh, M.H., Wang, W., 2019. Satellite surface soil moisture from SMAP, SMOS, AMSR2 and ESA CCI: a comprehensive assessment using global ground-based observations. Remote Sens. Environ. 231, 111215.

Meesters, A.G.C.A., Jeu, R.A.M.D., Owe, M., 2005. Analytical derivation of the vegetation optical depth from the microwave polarization difference index. IEEE Geosci. Remote Sens. Lett. 2, 121–123.

Mo, T., Choudhury, B.J., Schmugge, T.J., Wang, J.R., Jackson, T.J., 1982. A model for microwave emission from vegetation-covered fields. J. Geophys. Res. Oceans 87, 11229–11237.

Muñoz Sabater, J., 2019. ERA5-land hourly data from 1950 to present. In: Copernicus Climate Change Service (C3S) Climate Data Store (CDS).

Njoku, E.G., Chan, S.K., 2006. Vegetation and surface roughness effects on AMSR-E land observations. Remote Sens. Environ. 100, 190–199.

Njoku, E.G., Li, L., 1999. Retrieval of land surface parameters using passive microwave measurements at 6-18 GHz. IEEE Trans. Geosci. Remote Sens. 37, 79–93.
O'Neill, P., Chan, S., Bindlish, R., Chaubell, M., Colliander, A., Chen, F., Dunbar, S., Jackson, T., Peng, J., Cosh, M., Bongiovanni, T., Walker, J., Wu, X., Berg, A., McNairn, H., Thibeault, M., Fernández, J.M., González-Zamora, Á., Lopez-Baeza, E., Jensen, K., Seyfried, M., Bosch, D., Starks, P., Collins, C.H., Prueger, J., Su, Z., Velde, R.V.D., Asanuma, J., Palecki, M., Small, E., Zreda, M., Calvet, J., Crow, W., Kerr, Y., Yueh, S., Entekhabi, D., 2020. Soil Moisture Active Passive (SMAP) Project: Calibration and Validation for the L2/3_SM_P Version 7 and L2/3_SM_P_E Version 4 Data Products. Jet Propulsion Laboratory, Pasadena, CA.
O'Neill, P., Bindlish, R., Chan, S., Chaubell, J., Njoku, E., Jackson, T., 2021a. SMAP Algorithm Theoretical Basis Document. Level 2 & 3 Soil Moisture (Passive) Data Products.
O'Neill, P.E., Chan, S., Njoku, E.G., Jackson, T., Bindlish, R., Chaubell, J., 2021b. SMAP L3 Radiometer Global Daily 36 km EASE-Grid Soil Moisture, Version 8. NASA National Snow and Ice Data Center Distributed Active Archive Center, Boulder, Colorado USA.
Owe, M., Jeu, R.D., Walker, J., 2001. A methodology for surface soil moisture and vegetation optical depth retrieval using the microwave polarization difference index. IEEE Trans. Geosci. Remote Sens. 39, 1643–1654.
Parrens, M., Wigneron, J.-P., Richaume, P., Mialon, A., Al Bitar, A., Fernandez-Moran, R., Al-Yaari, A., Kerr, Y.H., 2016. Global-scale surface roughness effects at L-band as estimated from SMOS observations. Remote Sens. Environ. 181, 122–136.
Peng, B., Zhao, T., Shi, J., Lu, H., Mialon, A., Kerr, Y.H., Liang, X., Guan, K., 2017. Reappraisal of the roughness effect parameterization schemes for L-band radiometry over bare soil. Remote Sens. Environ. 199, 63–77.
Ramdas, A., Trillos, N.G., Cuturi, M., 2017. On Wasserstein two-sample testing and related families of nonparametric tests. Entropy 19.
Razavi, S., Jakeman, A., Saltelli, A., Prieur, C., Iooss, B., Borgonovo, E., Plischke, E., Lo Piano, S., Iwanaga, T., Becker, W., Tarantola, S., Guillaume, J.H.A., Jakeman, J., Gupta, H., Melillo, N., Rabitti, G., Chabridon, V., Duan, Q., Sun, X., Smith, S., Sheikholeslami, R., Hosseini, N., Asadzadeh, M., Puy, A., Kucherenko, S., Maier, H. R., 2021. The future of sensitivity analysis: an essential discipline for systems modeling and policy support. Environ. Model. Softw. 137, 104954.
Reiner, F., Brandt, M., Tong, X., Skole, D., Kariryaa, A., Ciais, P., Davies, A., Hiernaux, P., Chave, J., Mugabowindekwe, M., Igel, C., Oehmcke, S., Gieseke, F., Li, S., Liu, S., Saatchi, S., Boucher, P., Singh, J., Taugourdeau, S., Dendoncker, M., Song, X.-P., Mertz, O., Tucker, C.J., Fensholt, R., 2023a. Africa Tree Cover Map. Zenodo.
Reiner, F., Brandt, M., Tong, X., Skole, D., Kariryaa, A., Ciais, P., Davies, A., Hiernaux, P., Chave, J., Mugabowindekwe, M., Igel, C., Oehmcke, S., Gieseke, F., Li, S., Liu, S., Saatchi, S., Boucher, P., Singh, J., Taugourdeau, S., Dendoncker, M., Song, X.-P., Mertz, O., Tucker, C.J., Fensholt, R., 2023b. More than one quarter of Africa's tree cover is found outside areas previously classified as forest. Nat. Commun. 14, 2258.
Rodríguez-Fernández, N.J., Mialon, A., Mermoz, S., Bouvet, A., Richaume, P., Al Bitar, A., Al-Yaari, A., Brandt, M., Kaminski, T., Le Toan, T., Kerr, Y.H., Wigneron, J. P., 2018. An evaluation of SMOS L-band vegetation optical depth (L-VOD) data sets: high sensitivity of L-VOD to above-ground biomass in Africa. Biogeosciences 15, 4627–4645.
Runge, J., Gosling, W., Lezine, A.-M., Scott, L., 2022. Quaternary Vegetation Dynamics – The African Pollen Database.
Saleh, K., Wigneron, J.-P., de Rosnay, P., Calvet, J.-C., Escorihuela, M.J., Kerr, Y., Waldteufel, P., 2006. Impact of rain interception by vegetation and mulch on the L-band emission of natural grass. Remote Sens. Environ. 101, 127–139.
Santoro, M., Cartus, O., 2023. ESA Biomass Climate Change Initiative (Biomass_cci): global datasets of forest above-ground biomass for the years 2010, 2017, 2018, 2019 and 2020, v4. N.E.C.F.E.D. Analysis (Ed.).
Schaefer, G.L., Cosh, M.H., Jackson, T.J., 2007. The USDA Natural Resources Conservation Service Soil Climate Analysis Network (SCAN). J. Atmos. Ocean. Technol. 24, 2073–2077.
Schneeberger, K., Schwank, M., Stamm, C., de Rosnay, P., Mätzler, C., Flühler, H., 2004. Topsoil structure influencing soil water retrieval by microwave radiometry. Vadose Zone J. 3, 1169–1179.
Schwank, M., Matzler, C., Guglielmetti, M., Fluhler, H., 2005. L-band radiometer measurements of soil water under growing clover grass. IEEE Trans. Geosci. Remote Sens. 43, 2225–2237.
Schwank, M., Guglielmetti, M., Matzler, C., Fluhler, H., 2008. Testing a new model for the L-band radiation of moist leaf litter. IEEE Trans. Geosci. Remote Sens. 46, 1982–1994.
Schwank, M., Volksch, I., Wigneron, J.P., Kerr, Y.H., Mialon, A., Rosnay, P.D., Matzler, C., 2010. Comparison of two bare-soil reflectivity models and validation with L-band radiometer measurements. IEEE Trans. Geosci. Remote Sens. 48, 325–337.
Schwank, M., Kontu, A., Mialon, A., Naderpour, R., Houtz, D., Lemmetyinen, J., Rautiainen, K., Li, Q., Richaume, P., Kerr, Y., Mätzler, C., 2021. Temperature effects on L-band vegetation optical depth of a boreal forest. Remote Sens. Environ. 263, 112542.
Scott, D.W., 1979. On optimal and data-based histograms. Biometrika 66, 605–610.
Shi, J., Jackson, T., Tao, J., Du, J., Bindlish, R., Lu, L., Chen, K.S., 2008. Microwave vegetation indices for short vegetation covers from satellite passive microwave sensor AMSR-E. Remote Sens. Environ. 112, 4285–4300.
Su, Z., 2002. The Surface Energy Balance System (SEBS) for estimation of turbulent heat fluxes. Hydrol. Earth Syst. Sci. 6, 85–100.
Tian, F., Brandt, M., Liu, Y.Y., Verger, A., Tagesson, T., Diouf, A.A., Rasmussen, K., Mbow, C., Wang, Y., Fensholt, R., 2016. Remote sensing of vegetation dynamics in drylands: evaluating vegetation optical depth (VOD) using AVHRR NDVI and in situ green biomass data over West African Sahel. Remote Sens. Environ. 177, 265–276.
Ulaby, F.T., Wilson, E.A., 1985. Microwave attenuation properties of vegetation canopies. IEEE Trans. Geosci. Remote Sens. GE-23, 746–753.
Ulaby, F.T., Tavakoli, A., Thomas, B.A., 1987. Microwave propagation constant for a vegetation canopy with vertical stalks. IEEE Trans. Geosci. Remote Sens. GE-25, 714–725.
Van de Griend, A.A., Owe, M., Ruiter, J.D., Gouweleeuw, B.T., 1996. Measurement and behavior of dual-polarization vegetation optical depth and single scattering albedo at 1.4- and 5-GHz microwave frequencies. IEEE Trans. Geosci. Remote Sens. 34, 957–965.
Wang, J., Bras, R.L., 2011. A model of evapotranspiration based on the theory of maximum entropy production. Water Resour. Res. 47, W03521.
Wang, M., Fan, L., Frappart, F., Ciais, P., Sun, R., Liu, Y., Li, X., Liu, X., Moisy, C., Wigneron, J.-P., 2021. An alternative AMSR2 vegetation optical depth for monitoring vegetation at large scales. Remote Sens. Environ. 263, 112556.
Wang, H., Wigneron, J.-P., Ciais, P., Yao, Y., Fan, L., Liu, X., Li, X., Green, J.K., Tian, F., Tao, S., Li, W., Frappart, F., Albergel, C., Wang, M., Li, S., 2023. Seasonal variations in vegetation water content retrieved from microwave remote sensing over Amazon intact forests. Remote Sens. Environ. 285, 113409.
Wigneron, J.-P., Chanzy, A., Calvet, J.-C., Bruguier, N., 1995. A simple algorithm to retrieve soil moisture and vegetation biomass using passive microwave measurements over crop fields. Remote Sens. Environ. 51, 331–341.
Wigneron, J.P., Laguerre, L., Kerr, Y.H., 2001. A simple parameterization of the L-band microwave emission from rough agricultural soils. IEEE Trans. Geosci. Remote Sens. 39, 1697–1707.
Wigneron, J.P., Parde, M., Waldteufel, P., Chanzy, A., Kerr, Y., Schmidl, S., Skou, N., 2004. Characterizing the dependence of vegetation model parameters on crop structure, incidence angle, and polarization at L-band. IEEE Trans. Geosci. Remote Sens. 42, 416–425.
Wigneron, J.P., Jackson, T.J., O'Neill, P., De Lannoy, G., de Rosnay, P., Walker, J.P., Ferrazzoli, P., Mironov, V., Bircher, S., Grant, J.P., Kurum, M., Schwank, M., Munoz-Sabater, J., Das, N., Royer, A., Al-Yaari, A., Al Bitar, A., Fernandez-Moran, R., Lawrence, H., Mialon, A., Parrens, M., Richaume, P., Delwart, S., Kerr, Y., 2017. Modelling the passive microwave signature from land surfaces: a review of recent results and application to the L-band SMOS & SMAP soil moisture retrieval algorithms. Remote Sens. Environ. 192, 238–262.
Xu, X., Konings, A.G., Longo, M., Feldman, A., Xu, L., Saatchi, S., Wu, D., Wu, J., Moorcroft, P., 2021. Leaf surface water, not plant water stress, drives diurnal variation in tropical forest canopy water content. New Phytol. 231, 122–136.
Zhao, T., Shi, J., Lin, M., Yin, X., Liu, Y., Lan, H., Xiong, C., 2014. Potential soil moisture product from the Chinese HY-2 scanning microwave radiometer and its initial assessment. J. Appl. Remote. Sens. 8, 1–12.
Zhao, T.J., Shi, J.C., Rajat, B., Thomas, J., Michael, C., Jiang, L.M., Zhang, Z.J., Lan, H. M., 2015. Parametric exponentially correlated surface emission model for L-band passive microwave soil moisture retrieval. Phys. Chem. Earth 83-84, 65–74.
Zhao, T., Shi, J., Lv, L., Xu, H., Chen, D., Cui, Q., Jackson, T.J., Yan, G., Jia, L., Chen, L., Zhao, K., Zheng, X., Zhao, L., Zheng, C., Ji, D., Xiong, C., Wang, T., Li, R., Pan, J., Wen, J., Yu, C., Zheng, Y., Jiang, L., Chai, L., Lu, H., Yao, P., Ma, J., Lv, H., Wu, J., Zhao, W., Yang, N., Guo, P., Li, Y., Hu, L., Geng, D., Zhang, Z., 2020. Soil moisture experiment in the Luan River supporting new satellite mission opportunities. Remote Sens. Environ. 240, 111680.
Zhao, T., Shi, J., Entekhabi, D., Jackson, T.J., Hu, L., Peng, Z., Yao, P., Li, S., Kang, C.S., 2021. Retrievals of soil moisture and vegetation optical depth using a multi-channel collaborative algorithm. Remote Sens. Environ. 257, 112321.
Zheng, J., Zhao, T., Lü, H., Shi, J., Cosh, M.H., Ji, D., Jiang, L., Cui, Q., Lu, H., Yang, K., Wigneron, J.-P., Li, X., Zhu, Y., Hu, L., Peng, Z., Zeng, Y., Wang, X., Kang, C.S., 2022. Assessment of 24 soil moisture datasets using a new in situ network in the Shandian River Basin of China. Remote Sens. Environ. 271, 112891.
Zheng, J., Zhao, T., Lü, H., Zou, D., Rodriguez-Fernandez, N., Mialon, A., Richaume, P., Xiao, J., Ma, J., Fan, L., Song, P., Zhu, Y., Li, R., Yao, P., Yang, Q., Du, S., Wang, Z., Peng, Z., Xiong, Y., Xing, Z., Zhao, L., Kerr, Y., Shi, J., 2024. Use of a new Tibetan Plateau network for permafrost to characterize satellite-based products errors: an application to soil moisture and freeze/thaw. Remote Sens. Environ. 300, 113899.
Zwieback, S., Bosch, D.D., Cosh, M.H., Starks, P.J., Berg, A., 2019. Vegetation–soil moisture coupling metrics from dual-polarization microwave radiometry using regularization. Remote Sens. Environ. 231, 111257.